

1                   **Significant ionospheric hole and equatorial plasma**  
2                   **bubbles after the 2022 Tonga volcano eruption**

3                   **Ercha Aa<sup>1</sup>, Shun-Rong Zhang<sup>1</sup>, Philip J. Erickson<sup>1</sup>, Juha Vierinen<sup>2</sup>, Anthea J.**  
4                   **Coster<sup>1</sup>, Larisa P. Goncharenko<sup>1</sup>, Andres Spicher<sup>2</sup>, and William Rideout<sup>1</sup>**

5                   <sup>1</sup>Haystack Observatory, Massachusetts Institute of Technology, Westford, MA, USA.

6                   <sup>2</sup>Department of Physics and Technology, The Arctic University of Norway, Tromsø, Norway

7                   **Key Points:**

- 8                   • Shock-acoustic impulses created a significant ionospheric hole of 10+ TECU de-  
9                   pletion near the epicenter, with an estimated radius of 10-15°  
10                  • Pronounced post-volcanic equatorial plasma bubbles were continuously developed  
11                  across the Asia-Oceania area covering ~140° longitudes  
12                  • Strong plasma bubbles were likely triggered by gravity wave resonance with Lamb  
13                  waves and volcano-increased PRE/PSSR of equatorial F-layer

---

Corresponding author: E. Aa, [aercha@mit.edu](mailto:aercha@mit.edu)

## Abstract

This paper investigates the local and global ionospheric responses to the 2022 Tonga volcano eruption, using ground-based Global Navigation Satellite System (GNSS) total electron content (TEC), Swarm in-situ plasma density measurements, the Ionospheric Connection Explorer (ICON) Ion Velocity Meter (IVM) data, and ionosonde measurements. The main results are as follows: (1) A significant local ionospheric hole of more than 10 TECU depletion was observed near the epicenter  $\sim 45$  min after the eruption, comprising of several cascading TEC decreases and quasi-periodic oscillations. Such a deep local plasma hole was also observed by space-borne in-situ measurements, with an estimated horizontal radius of  $10\text{--}15^\circ$  and persisted for more than 10 hours in ICON-IVM ion density profiles until local sunrise. (2) Pronounced post-volcanic evening equatorial plasma bubbles (EPBs) were continuously observed across the wide Asia-Oceania area after the arrival of volcano-induced waves; these caused a  $N_e$  decrease of 2–3 orders of magnitude at Swarm/ICON altitude between 450–575 km, covered wide longitudinal ranges of more than  $140^\circ$ , and lasted around 12 hours. (3) Various acoustic-gravity wave modes due to volcano eruption were observed by accurate Beidou geostationary orbit (GEO) TEC, and the huge ionospheric hole was mainly caused by intense shock-acoustic impulses. TEC rate of change index revealed globally propagating ionospheric disturbances at a prevailing Lamb-wave mode of  $\sim 315$  m/s; the large-scale EPBs could be seeded by acoustic-gravity resonance and coupling to less-damped Lamb waves, under a favorable condition of volcano-induced enhancement of dusktime plasma upward  $E \times B$  drift and postsunset rise of the equatorial ionospheric F-layer.

## Plain Language Summary

The catastrophic 2022 Tonga volcano eruption triggered giant atmospheric waves that propagated into and strongly impacted Earth’s ionosphere. Using ground-based multi-GNSS TEC and ionosonde measurements as well as space-borne Swarm and ICON satellites observations, we found large-scale, intense ionospheric disturbances. The eruption created a large ionospheric hole near the epicenter embedded with cascading TEC drops and periodic oscillations, resulting from various shock-acoustic wave impulses. Atmospheric Lamb waves propagated globally at a velocity of  $\sim 315$  m/s, coupled to ionosphere heights possibly via acoustic-gravity resonance, and caused global-scale ionospheric disturbances. We report for the first time that strong nighttime equatorial plasma bubbles were continuously observed over the vast Asia-Oceania area of more than  $140^\circ$  longitudinal range, lasting around 12 hours following the consecutive arrival of volcano-induced waves and the dusk terminator. These results demonstrate far-reaching and long-lasting atmosphere-ionosphere impacts from a devastating natural disaster, and highlight new ways in which surface conditions can impact the upper atmosphere.

## 1 Introduction

Natural geological disasters such as volcanic eruptions and intense earthquakes can create impulsive forcing near Earth’s surface and cause considerable atmospheric pressure waves (e.g., Hines, 1960; Yeh & Liu, 1974; Komjathy et al., 2016). Depending on their velocities and/or frequencies, these atmospheric waves include supersonic shock waves along with acoustic and gravity waves (AGWs). Acoustic waves travel through adiabatic compression and decompression, with frequencies higher than the acoustic cutoff frequency ( $\sim 3.3$  mHz), periods smaller than 5 min, and radially outward propagating velocity at the sound speed (Astafyeva, 2019; E. Blanc, 1985). By comparison, gravity waves are triggered by vertical displacement in the ocean surface and atmosphere, with gravity being the predominant restoring force. They are characterized by lower-than-buoyancy frequencies, periods of several to tens of minutes, and obliquely upward propagating pattern with oppositely directed phase and group velocities (Artru et al., 2004; C. Y. Huang

64 et al., 2019). The initial AGWs generated by these events can even reach ionospheric heights  
 65 with exponentially-increased amplitudes, modulating ionospheric electron density lead-  
 66 ing to traveling ionospheric disturbances (TIDs) through ion-neutral collisional momen-  
 67 tum transfer (e.g., Afraimovich et al., 2010; Cahyadi & Heki, 2013; Chou et al., 2020;  
 68 Dautermann, Calais, & Mattioli, 2009; Hao et al., 2006; Huba et al., 2015; Inchin et al.,  
 69 2020; Komjathy et al., 2012; J. Y. Liu et al., 2006; Nishioka et al., 2013; Rolland et al.,  
 70 2011; Tsugawa et al., 2011; Zettergren et al., 2017).

71 The rapid development over the past few decades of ground-based Global Naviga-  
 72 tion Satellite System (GNSS) receiver networks has allowed ionospheric responses to volcano-  
 73 induced AGWs to be intermittently investigated based on sporadic eruption events. For  
 74 instance, Roberts et al. (1982) found that ionospheric TIDs after the explosion of Mount  
 75 St. Helens were detected 4900 km away with various propagation velocities between 350–  
 76 550 m/s. C. H. Liu et al. (1982) found that some atmospheric perturbations for this same  
 77 event were capable of travelling globally in the form of Lamb waves. Moreover, Heki (2006)  
 78 observed that ionospheric total electron content (TEC) disturbances triggered by acous-  
 79 tic waves after the Asamo volcano eruption could propagate as fast as 1.1 km/s. Dautermann,  
 80 Calais, and Mattioli (2009) and Dautermann, Calais, Lognonné, and Mattioli (2009) found  
 81 that quasiperiodic TEC oscillations around 4 mHz were detected 18 min after the Soufrière  
 82 Hill Volcano explosion and lasted 40 min, with various horizontal velocities between 500–  
 83 700 m/s. Shults et al. (2016) observed that the propagation velocity of ionospheric TEC  
 84 disturbances after the Calbuco volcano eruption was around 900–1200 m/s, close to acous-  
 85 tic speeds at ionospheric heights. Nakashima et al. (2016) found that harmonic acous-  
 86 tic oscillations created by the Kelud volcano eruption lasted for 2.5 hr with ionosphere  
 87 disturbances traveling at 800 m/s. These studies in aggregate have greatly informed com-  
 88 munity knowledge of co-volcanic ionospheric disturbances.

89 The recent Hunga Tonga-Hunga Ha’apai (herein simplified as Tonga) volcano erup-  
 90 tion at 04:14:45 UT on 15 January 2022 was the largest eruption in the last three decades,  
 91 causing significant wave perturbations from ocean surface to the whole atmosphere across  
 92 the globe in less than 24 hours (Duncombe, 2022). This event provides a unique scien-  
 93 tific opportunity to advance the current understanding of volcano-induced local and global  
 94 ionospheric responses. So far, prompt studies have provided some initial analyses of iono-  
 95 spheric disturbances after eruption. For example, Themens et al. (2022) analyzed regional  
 96 and global large-scale and medium-scale TID features following the eruption; Zhang et  
 97 al. (2022) found global propagation of Lamb waves for three full cycles within four days;  
 98 Lin et al. (2022) reported rapid appearance of disturbances in the conjugate Hemisphere;  
 99 Harding et al. (2022) found that strong horizontal neutral wind perturbations due to vol-  
 100 cano eruption could considerable modify equatorial electric field.

101 Despite these important early results, more features of this event remain to be an-  
 102 alyzed. In this study, we use ground-based GNSS TEC data, satellite in-situ measure-  
 103 ments from Swarm and ICON, and ionosonde measurements to investigate two new phe-  
 104 nomena associated with the Tonga volcano eruption: (1) A significant ionospheric plasma  
 105 hole was observed near the eruption epicenter with a depletion magnitude of more than  
 106 10 TECU and a horizontal radius of 10–15°. (2) Pronounced post-volcanic evening equa-  
 107 torial plasma bubbles (EPBs) were continuously observed across a wide Asia-Oceania  
 108 area of  $\sim 140^\circ$  longitudes following the arrival of Lamb waves, with magnitude decreased  
 109 by 2-3 orders and lasted around 12 hours. In particular, this is the first time such dra-  
 110 matic plasma density depletion associated with volcano-induced AGWs has been reported.  
 111 Our study also uses Beidou Geostationary Orbit (GEO) data for precise TEC measure-  
 112 ments at stationary ionosphere pierce points (IPPs) near Tonga and accurate analysis  
 113 of local ionospheric disturbances. These results are discussed in the following sections.

## 114 2 Instruments and Data Description

115 Ground-based GNSS TEC data are produced at the Massachusetts Institute of Tech-  
 116 nology’s Haystack Observatory using 5000+ worldwide GNSS receivers, and are provided  
 117 through the Madrigal distributed data system (Rideout & Coster, 2006; Vierinen et al.,  
 118 2016). Besides traditional GPS/GLONASS TEC, we also used TEC from 240+ avail-  
 119 able Beidou receivers, especially from Beidou GEO receivers adjacent to eruption. Bei-  
 120 dou GEO TEC data can provide more robust estimation from stationary IPPs in a man-  
 121 ner less impacted by complicated ionospheric spatiotemporal variability. In addition to  
 122 the absolute TEC, we also used two other quantities to investigate ionospheric response  
 123 to the eruption: (1) Detrended TEC (dTEC), characterizing the wave-like ionospheric  
 124 oscillations by removing a background variation trend for all satellite-receiver TEC pairs.  
 125 Detrending is performed using a Savitzky-Golay low-pass filter with a 30-min sliding win-  
 126 dow (Savitzky & Golay, 1964; Zhang et al., 2017, 2019). (2) Rate of TEC Index (ROTI),  
 127 describing dynamic ionospheric changes due to plasma irregularities and/or gradients.  
 128 ROTI is defined as the 5-min standard deviation of the TEC time derivative (Pi et al.,  
 129 1997; Cherniak et al., 2014; Aa et al., 2019).

130 Besides ground-based GNSS TEC, we also used in-situ electron density ( $N_e$ ) mea-  
 131 surements from the European Space Agency’s Swarm constellations (Friis-Christensen  
 132 et al., 2008; Spicher et al., 2015). Swarm includes three identical satellites that fly in ap-  
 133 proximately circular orbits at  $88^\circ$  inclination. Swarm A and C fly side-by-side at around  
 134 450 km with  $1.4^\circ$  longitudinal separation, and Swarm B fly at around 510 km (Knudsen  
 135 et al., 2017).

136 ICON is a low-Earth orbit satellite for ionospheric and thermospheric measurements  
 137 that flying at an altitude of 575 km with an inclination angle of  $27^\circ$  (Immel et al., 2018).  
 138 ICON carries Ion Velocity Meter (IVM) instruments that consists of the Retarding Po-  
 139 tential Analyzer (RPA) and the Drift Meter (DM), which collectively provide ion den-  
 140 sity, the major ion composition, the ion temperature, and the ion velocity measurements  
 141 (Heelis et al., 2017). In this study, we use ICON-IVM ion density and velocity measure-  
 142 ments to analyze the volcano-related ionospheric disturbances.

143 Moreover, the infrared brightness cloud temperature data, derived from Geosyn-  
 144 chronous Operational Environmental Satellites (GOES) and other selected geostation-  
 145 ary satellites (Janowiak et al., 2017), were also used to gauge volcano-related convection  
 146 activity. Equatorial ionosonde measurements of F2-layer peak height (hmF2) and elec-  
 147 tron density profiles at GUAM ( $13.62^\circ\text{N}$ ,  $144.86^\circ\text{E}$ ) are also utilized.

## 148 3 Results

### 149 3.1 Local Ionospheric Disturbances

150 Figure 1a shows the volcano epicenter location ( $20.5^\circ\text{S}$ ,  $175.4^\circ\text{W}$ ) and the great-  
 151 circle distances from the epicenter at an ionospheric height of 300 km. Also shown are  
 152 four adjacent Beidou GEO receivers within 1000 km radius: TONG ( $21.02^\circ\text{S}$ ,  $175.18^\circ\text{W}$ ),  
 153 LAUT ( $17.5^\circ\text{S}$ ,  $177.45^\circ\text{E}$ ), SAMO ( $13.76^\circ\text{S}$ ,  $171.74^\circ\text{W}$ ), and FTNA ( $14.22^\circ\text{S}$ ,  $178.12^\circ\text{W}$ ).  
 154 Figure 1b shows a regional view with overlaid infrared brightness cloud temperature at  
 155 05 UT on 15 January 2022. The dark blue region over Tonga indicates a newly-formed  
 156 cold area with cloud temperature below 220 K. This was about 80–100 K lower than 1  
 157 hour ago, which indicates that the initial ash plume had protruded rapidly into the tropopause  
 158 in less than 45 mins triggering considerable atmospheric cooling. Also shown are fixed  
 159 IPPs locations of Beidou GEO satellites C01 and C04 for each receiver.

160 The unique Beidou GEO observations with stationary IPPs allow us to accurately  
 161 determine localized temporal ionospheric variations following the eruption (Figures 1c–  
 162 1f). At TONG, the nearest station to the epicenter, after a minor increase following the

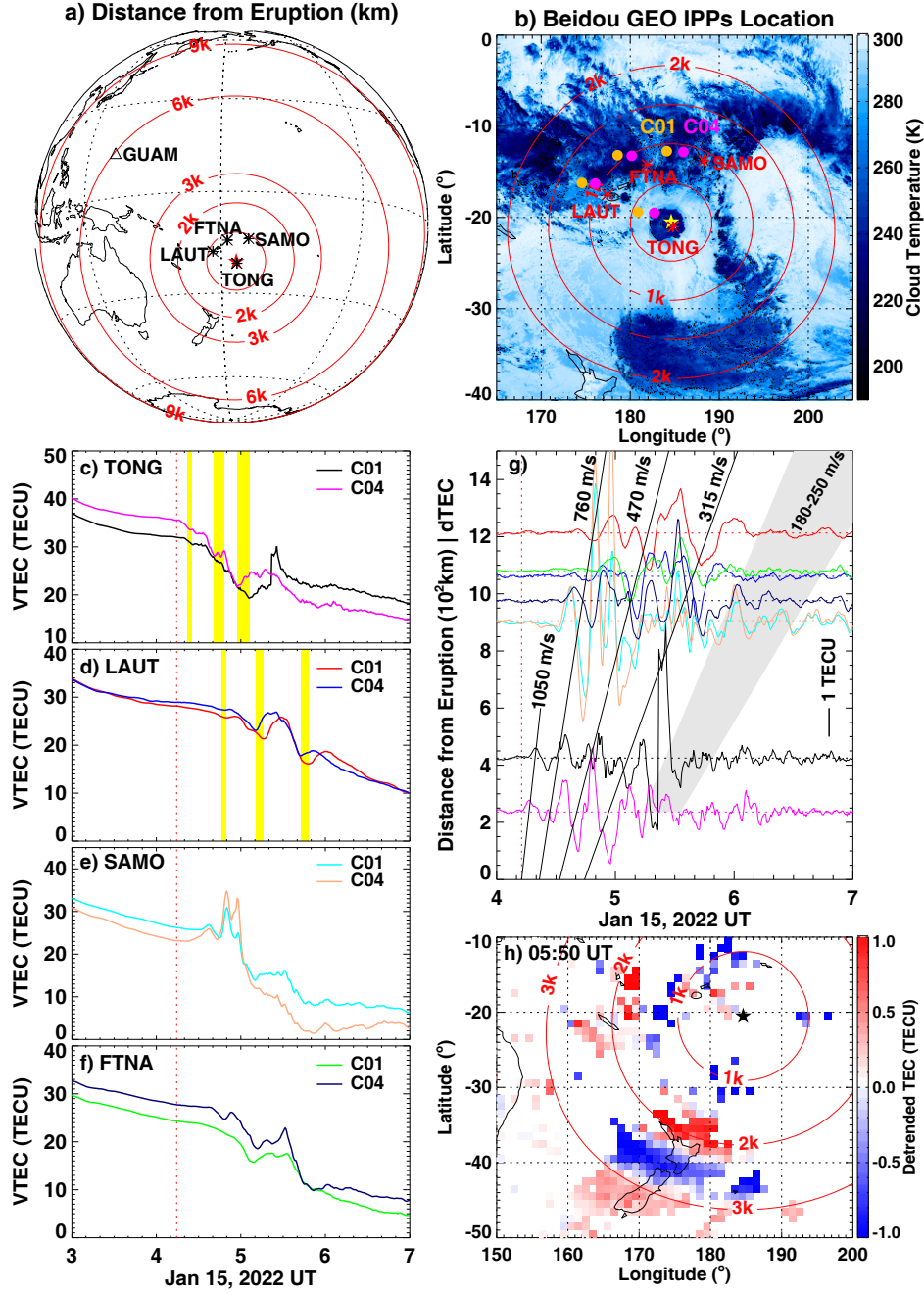


**Figure 1.** (a) Global view of the Tonga volcano eruption location (star), four adjacent Beidou GEO receivers (asterisks), and an ionosonde (triangle). The iso-distance circles from the eruption epicenter are shown in red lines. (b) Regional view of above-mentioned information and corresponding Beidou GEO IPPs location for C01 and C04 satellites, overlaid with the deep cloud brightness temperature observations at 05 UT on 15 January 2022. (c–f) Temporal variation of Beidou GEO TEC at four sites. The eruption time is marked by a vertical dotted line. Yellow shades mark three distinct TEC dips using TONG and LAUT measurements as examples. (g) UT-distance variation of detrended Beidou GEO TEC. The vertical line indicates eruption beginning time; the slanted lines and shades indicate different propagation velocities. (h) Observation of concentric TIDs near New Zealand using two-dimensional detrended TEC map.

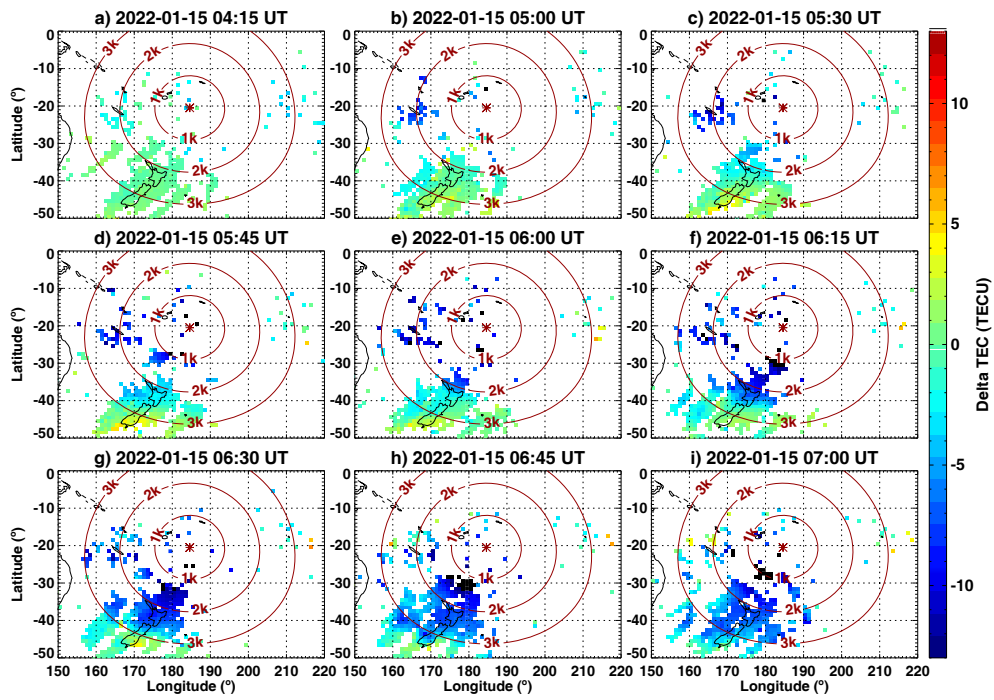


**Figure 2.** (a–i) Regional two-dimensional delta TEC maps in the vicinity of volcanic eruption between 04:15–07:00 UT on January 15. The iso-distance lines from the eruption epicenter (asterisk) are shown in red circles.

163 eruption, the TEC curves showed three major cascading dips as marked by yellow shades.  
 164 Collectively these formed an integrated depletion hole around 05 UT with a depletion  
 165 amplitude of around 10 TECU. Smaller-scale periodic oscillations were also detected to  
 166 embed in the depletion. Similar to TONG, LAUT TEC curves also exhibited three con-  
 167 secutive dips shortly after the eruption, with a clear phase and time delay between C01  
 168 and C04 among TONG and LAUT. Since fixed IPP locations from TONG and LAUT  
 169 (corresponding to C01 and C04) were approximately arrayed radially outward in the same  
 170 direction away from the epicenter (Figure 1b), we can collectively utilize their distance  
 171 and phase/time information to deduce wave propagation parameters in this localized re-  
 172 gion. For SAMO and FTNA, the radial distances of their GEO IPPs were close, which  
 173 made accurate detection of oscillation phase and time delay a little bit difficult compared  
 174 to TONG and LAUT. Nevertheless, immense depletion features can also be seen at SAMO  
 175 and FTNA through cliff-like TEC drops as large as 10–15 TECU, and were particularly  
 176 prominent over SAMO around 5 UT. This volcano-induced effect was much earlier be-  
 177 fore local sunset around 0620–0700 UT,

178 To further extract wave-like oscillations embedded in the depletion, Figure 1g plots  
 179 all detrended Beidou GEO TEC curves in UT-distance coordinates. Volcano-induced fluc-  
 180 tuations were generally within 0.5-3 TECU but sometimes reached 6 TECU. Recall from  
 181 above that the TEC curves at TONG and LAUT showed three cascading dips as marked  
 182 by yellow shades, thus the propagating velocities can be estimated using detrended TEC  
 183 through slanted fiducial lines to connect iso-phase points at the valley for each dip from  
 184 the same static IPP C01 and C04 between TONG and LAUT. The radial propagation  
 185 velocity corresponding to these three major dips were calculated to be 760 m/s, 470 m/s,  
 186 and 315 m/s, respectively. Specifically, taking the 315 m/s fiducial line as an example,  
 187 we used detrended Beidou GEO TEC to search the time point when C01 TEC at TONG  
 188 (black curve) and C01 TEC at LAUT (red curve) reached their respective local mini-  
 189 mum point within the third major dip: 05:06:30 UT and 05:48:00 UT. Thus the prop-  
 190 agation velocity in this region can be calculated using their IPP distance and time dif-  
 191 ference information, which was estimated to be 316.4 m/s. Similarly, when C04 satel-  
 192 lite was used for the calculation, the estimated propagation velocity was 312.5 m/s. Taken  
 193 as a whole, the fiducial line was estimated to be  $\sim 315$  m/s. Moreover, some smaller-scale  
 194 oscillations with velocities of 180-250 m/s were registered after major perturbations. If  
 195 considering TONG measurements alone, another fast travelling wave mode with 1050 m/s  
 196 speed can be derived by connecting two initial dTEC bumps at C01 and C04, though  
 197 this fast wave did not seem to propagate beyond 1000 km.

198 We here mainly use TONG and LAUT to derive the fiducial lines since their cor-  
 199 responding IPPs are approximately radial outward aligned with respect to the eruption  
 200 epicenter. There are some modest variations if using other pairs to do the calculate, say  
 201 using TONG and SAMO, possibly due to their respective IPP points and epicenter are  
 202 not aligned in a line, considering that the wave propagation could be un-isotropic in dif-  
 203 ferent direction. Despite fewer Beidou GEO observations as compared to GPS, these es-  
 204 timations have the key quality of being free from possible spatiotemporal variation con-  
 205 tamination associated with normal moving IPPs. The estimated onset times of these con-  
 206 tinuous perturbations are marked in the horizontal axis of Figure 1g, which are similar  
 207 to those derived in Astafyeva et al. (2022) using TONG-FTNA station pairs with multi-  
 208 GNSS measurements. In addition, within the eruption near field, Figure 1h displays a  
 209 2-D dTEC map combining multi-GNSS measurements to show concentric TID features  
 210 over New Zealand at 2000-3000 km distance with an estimated wavelength of 1200-1500 km.  
 211 These characteristics are generally consistent with recent studies (e.g., Themens et al.,  
 212 2022; Zhang et al., 2022) and will not be described further in this study.

213 The local ionospheric hole of TEC depletion in the vicinity of the eruption center  
 214 can also be observed in 2-D delta TEC maps at different time steps between 04:15–07:00 UT  
 215 on January 15 as shown in Figure 2. The delta TEC values were calculated by subtract-

216 ing averaged TEC values of three geomagnetically quiet reference days (January 11–13)  
 217 before the volcano eruption. Despite some data gaps near epicenter, the delta TEC re-  
 218 sults clearly demonstrated the evolution of local depletion structures. The signature of  
 219 ionospheric hole can be seen around 05 UT near epicenter with sporadic points of TEC  
 220 depletion for 5–10 TECU. This depletion continued for at least two hours and extended  
 221 outward forming a huge ionospheric hole with its magnitude reaching more than 10 TECU  
 222 even around 2000 km away (Figures 2f–2h). The horizontal scale and magnitude of such  
 223 a huge ionospheric hole is quite unique and impressive, which are much stronger than that  
 224 of the famous Tohoku Earthquake-induced local ionospheric hole with 5–6 TECU de-  
 225pletion and horizontal size of 500 km (e.g., Tsugawa et al., 2011; Saito et al., 2011). The  
 226 mechanisms of this local ionospheric hole will be further discussed in Section 4.

### 227 3.2 Global Ionospheric Disturbances with Strong EPBs

228 Besides significant local depletion, ionospheric ripples also propagated globally. Fig-  
 229 ures 3a and 3b show two examples of 2-D global ROTI maps on 15 January 2022 derived  
 230 from 5000+ multi-GNSS receivers. At 12:00 UT, large ROTI values manifesting strong  
 231 ionospheric irregularities were widely registered in the low and midlatitude East Asian  
 232 sector around 6000–9000 km distance. At 14:00 UT, beside the Asian sector, noticeable  
 233 gradients features were simultaneously found both in the North and South American area  
 234 approximately parallel to the 12,000 km iso-distance line therein. To zoom in the prop-  
 235 agation feature, Figures 3c–3h display six consecutive ROTI maps over North Ameri-  
 236 can sector between 13:30–16:00 UT. The wavefront propagation signatures can be clearly  
 237 seen via eastward structure movement in higher-than-background ROTI values that ap-  
 238 proximately parallel to iso-distance lines, which were marked with red arrows. The wave-  
 239 fronts propagated outbound from  $\sim 11,000$  km to  $\sim 14,000$  km with an average velocity  
 240 of 315 m/s, consistent with one propagation mode in Beidou TEC results (Figure 1g).  
 241 The full animation of global ROTI variation is attached in the supplementary material.

242 For widespread irregularity features in the Asian sector, Figures 3i–3n show six ROTI  
 243 maps therein between 11–16 UT. Ionospheric irregularities were quite noticeable around  
 244 the equatorial ionization anomaly (EIA) crests, which extended westbound from Indone-  
 245 sia, Philippines, and the Japan archipelago around 11:00 UT all the way to India and  
 246 the Bay of Bengal around 15–16 UT. Moreover, to provide a global synoptic view with  
 247 extended spatial/temporal ROTI coverage and to utilize space-borne observations, Fig-  
 248 ures 4a–4h show sixteen consecutive paths of Swarm C (blue) and Swarm B (red) satel-  
 249 lites that flew in the pre-midnight local time sector of 23 LT over Asia-Oceania area, over-  
 250 laying on top of eight background ROTI maps between 08:30–19:30 UT on January 15.  
 251 The iso-distance lines away from the eruption epicenter are shown by black circles with  
 252 the anticipated wavefront of Lamb waves being marked by a green circle. The right pan-  
 253 els in each subfigure display the corresponding geomagnetic latitudinal profiles of in-situ  
 254  $N_e$  for Swarm C (even number) and Swarm B (odd number) paths, respectively. The ref-  
 255 erence background  $N_e$  profiles from the day before (dotted lines) and after (dashed lines)  
 256 were also plotted for comparison. The westbound phase extension of locally-developed  
 257 plasma irregularity features shown by high ROTI values is generally in concert with the  
 258 anticipated Lamb waves propagation. Moreover, the volcano-induced local and global  
 259 ionospheric disturbances can also be derived from Swarm plasma density profiles. At 08:30 UT  
 260 (Figure 4a), Swarm B and C were flying on the eastern side of the volcanic eruption epi-  
 261 center about  $30\text{--}40^\circ$  longitude away, which did not detect considerable plasma irregu-  
 262 larities. At 10 UT (Figure 4b), Swarm C was flying around  $167.8^\circ\text{W}$  longitude, merely  
 263  $7\text{--}8^\circ$  from that of the volcanic eruption. A broad equatorial plasma depletion with a lat-  
 264 itudinal width of  $20\text{--}25^\circ$  was registered in Swarm C Path 02 comprising of smaller-scale  
 265 plasma irregularities, in which the plasma density was reduced by 2–3 orders of magni-  
 266 tude reaching as low as  $10^2\text{ cm}^{-3}$ . Such a broad equatorial plasma depletion suggests  
 267 that the equatorial ionospheric height was significantly uplifted near the volcanic erup-  
 268 tion longitude possibly by enhanced fountain effect, so that the satellite might fly be-

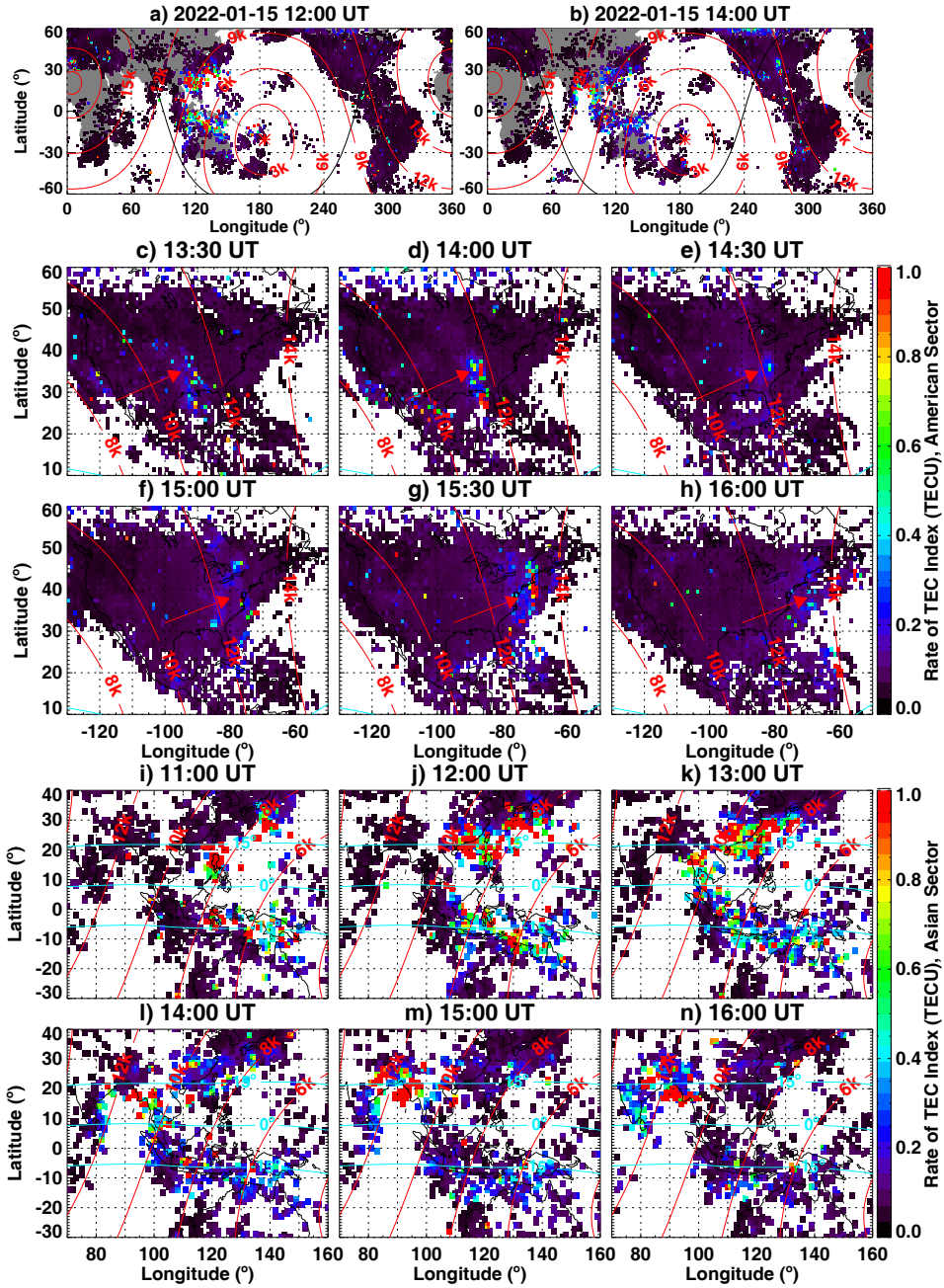


**Figure 3.** (a and b) Global 2-D ROTI maps at 12 UT and 14 UT on January 15. The volcano eruption location (asterisk), iso-distance lines from eruption (red lines), and solar terminator (black line) are marked. (c–h) Regional ROTI maps over North American between 13:30–16:00 UT. The red arrows mark the propagation of volcano-induced wavefront. (i–n) Regional ROTI maps over Asian sectors between 11–16 UT. The iso-distance lines from eruption (red lines) and geomagnetic equator and  $\pm 15^\circ$  lines (cyan) are marked.

low the F2-region peak height while crossing the equatorial region to encounter low-density trough (Kil & Lee, 2013; Lee et al., 2014). At 11:30 UT (Figure 4c), Swarm C and B were flying across the western side of volcanic eruption around 168.8°E and 179.2°E longitudes, respectively. As can be seen, significant equatorial and low-latitude plasma bite-outs with the density as low as  $10^2$ – $10^3$  cm<sup>-3</sup> were quite obvious in both profiles, which were 2–3 orders of magnitude lower than reference levels. The irregularity activity on reference days is much weaker. Besides noticeable plasma bubbles, a significant feature of the local ionospheric hole was also registered in Swarm B profile of Path 03 between 20–40°S geomagnetic latitude, thus the latitudinal radius of the ionospheric hole was estimated to be  $\sim 10^\circ$  that consistent with TEC measurements in Figure 2. In the following time steps, similar signatures of strong plasma bubbles can also be consecutively observed by Swarm satellites across Papua New Guinea (Figure 4d), East Asia (Figure 4e), Indonesia (Figure 4f), India (Figure 4g), and even partially east African sector (Figure 4h). These ground-based GNSS ROTI and space-borne in-situ  $N_e$  data collectively indicate that strong post-volcanic EPBs continuously developed across a wide Asian sector covering more than 140° longitudes at local postsunset period on January 15. This is reported for the first time after an extreme volcano eruption.

The latitudinal/altitudinal extension of these post-volcanic EPBs is also worth discussion. In particular, Swarm profiles in Figure 4e showed that EPBs likely extended to  $\pm 20$ – $25^\circ$  geomagnetic latitudes (MLAT) in East Asian sector, indicating that the Apex height of these EPBs may reach  $\sim 1500$  km above the equator. This is quite similar to those shown in Shiokawa et al. (2004), suggesting a large upward plasma drift speed in the equatorial region. Similar high-altitude EPBs were occasionally observed in the literature. For example, Ma and Maruyama (2006) found that EPBs could be observed at  $31^\circ$  MLAT in GNSS TEC observations; Foster and Rich (1998) reported that EPB signatures could be observed by Millstone Hill incoherent scatter radar at  $35$ – $37^\circ$  MLAT; Katamzi-Joseph et al. (2017) and Cherniak and Zakharenkova (2016) reported that EPBs can extend to  $40^\circ$  MLAT in Europe using ground-based TEC and in-situ measurements. (Aa et al., 2019) found that bubble-like ionospheric depletion structures could expand to much higher latitudes of  $46^\circ$  MLAT that map to Apex height of more than 6000 km. In contrast, the latitude/altitude extension of these post-volcanic EPBs reported in this study is smaller than and different from those storm-induced super plasma bubbles.

To better investigate the EPBs' evolution and their connection to volcano-induced waves, Figures 5a–5d show original TEC keograms as a function of time and longitude along  $20^\circ$ N (the approximate latitudinal location of northern EIA crest over the Asian sector) during January 13–16, respectively. The EIA crest morphology on January 15 (Figure 5c) was considerably different from the other reference days with more natural variation. In particular, the EIA crest intensity on January 15 was significantly eroded by more than 10 TEC unit between 09–14 UT, with a sharp edge following the consecutive passage of dusk terminator and anticipated westward-propagating Lamb wave from 6,000 km to 12,000 km that marked by a red arrow. The disturbance propagating speed was estimated to be 310–350 m/s that consistent with the estimated atmospheric Lamb wave velocity from recent studies (Themens et al., 2022; Zhang et al., 2022). Most importantly, shortly after the passage of disturbed TEC depletion, noticeable low-density dark streaks representing EPBs with comb-like periodic longitudinal distribution (shown by quasi-parallel black dashed lines) were developed and embedded within the partially-recovered EIA crest. The inter-bubble distance was estimated to be around 400–900 km, similar to those indicated in previous studies on periodic EPBs structures (e.g., Aa, Zou, Eastes, et al., 2020; Das et al., 2020; Makela et al., 2010; Huba & Liu, 2020; Takahashi et al., 2015). These notable features of EIA bite-out and periodic EPBs after the passage of Lamb waves provide important evidence of the novel linkage between volcano eruption and ionospheric disturbances, which will be further discussed in the next section.

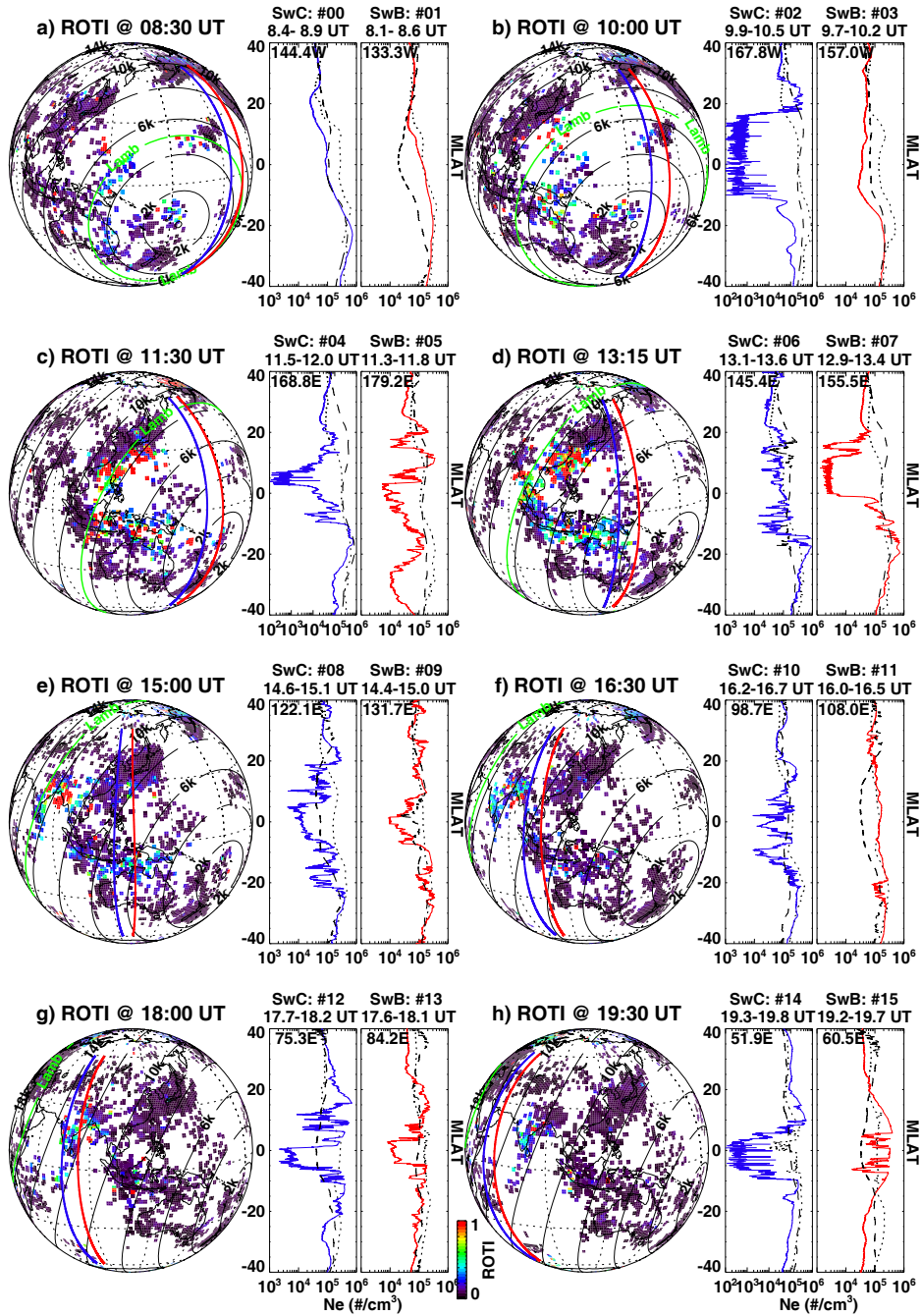


**Figure 4.** (a–h) Global ROTI maps focusing on Asia–Oceania sector at eight time steps between 08:30–19:30 UT on 15 January 2022 with overlapping Swarm C (blue) and Swarm B (red) paths. The iso-distance lines from eruption are marked with black circles. A green circle marks the anticipated wavefront propagation of atmospheric Lamb waves. The right two panels in each sub-figure show corresponding electron density variation as a function of geomagnetic latitudes along Swarm paths around 23 LT. The path are marked with even (odd) numbers for Swarm C (B). The black dotted and dashed lines show corresponding reference profiles from the day before and after the volcano eruption, respectively.

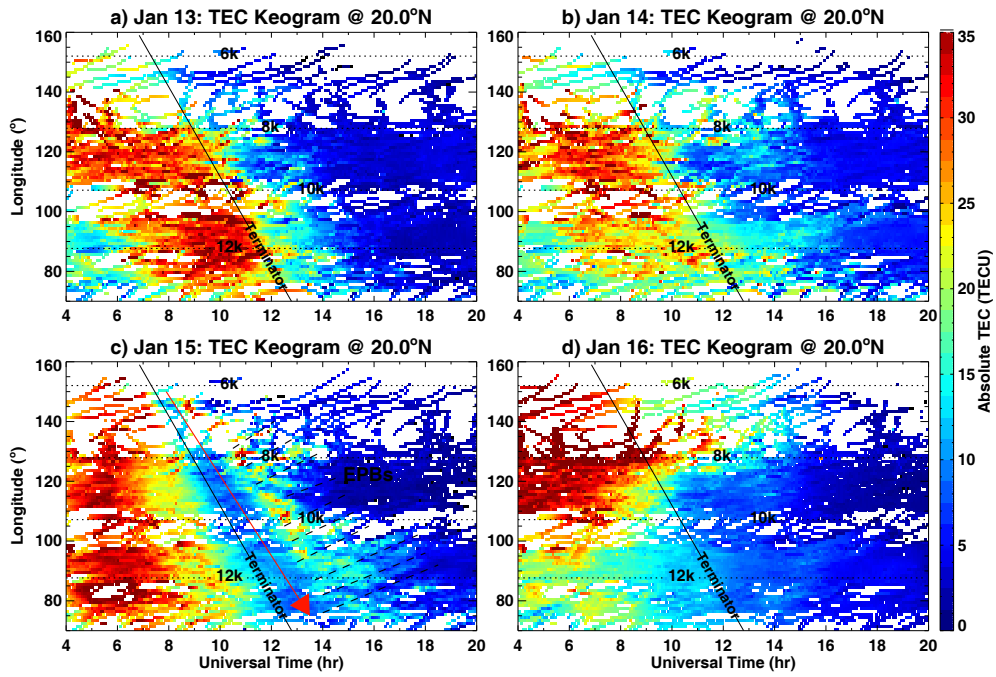


**Figure 5.** (a–d) TEC keograms as a function of time and longitude along  $20^\circ$  latitude during January 13–16, respectively. The terminator (solid lines) and iso-distance lines (dotted) from volcano eruption are also shown. The red arrow in Figure 5c marks a significant TEC erosion following the anticipated Lamb wave passage. Quasi-parallel dashed lines in Figure 5c mark quasi-periodic EPBs that embedded within the EIA crest.

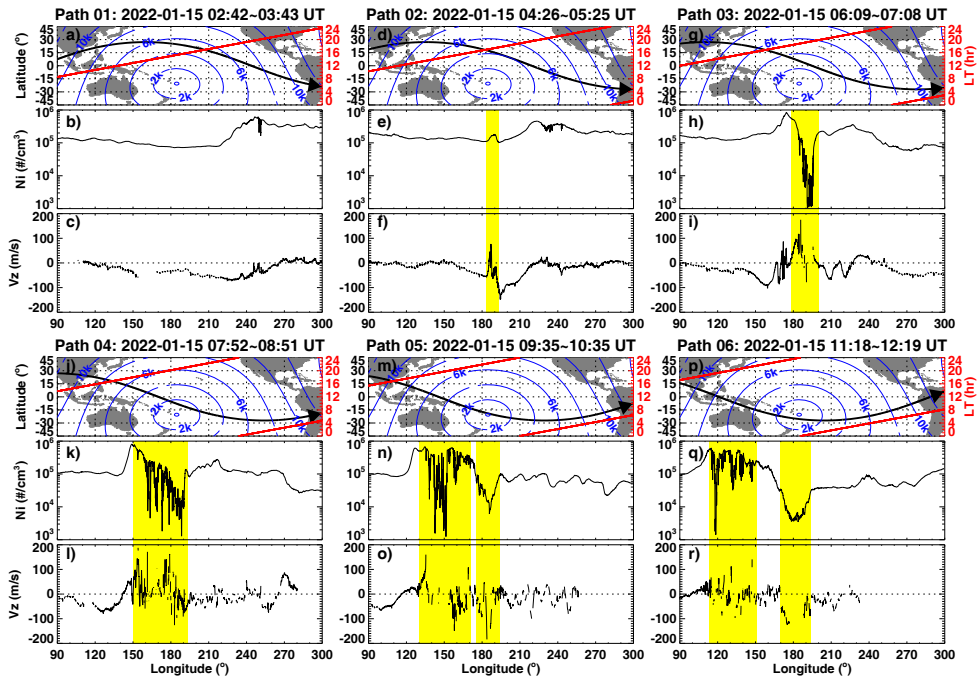


**Figure 6.** (a–r) ICON-IVM observation tracks and corresponding local time, ion density, and vertical drift results for six consecutive paths between 02:42–12:19 UT on 15 January 2022. Iso-distance lines away from the Tonga volcano eruption epicenter with 2000 km interval are also marked on maps. The shaded regions mark noticeable plasma density and/or drift disturbances after the volcano eruption.

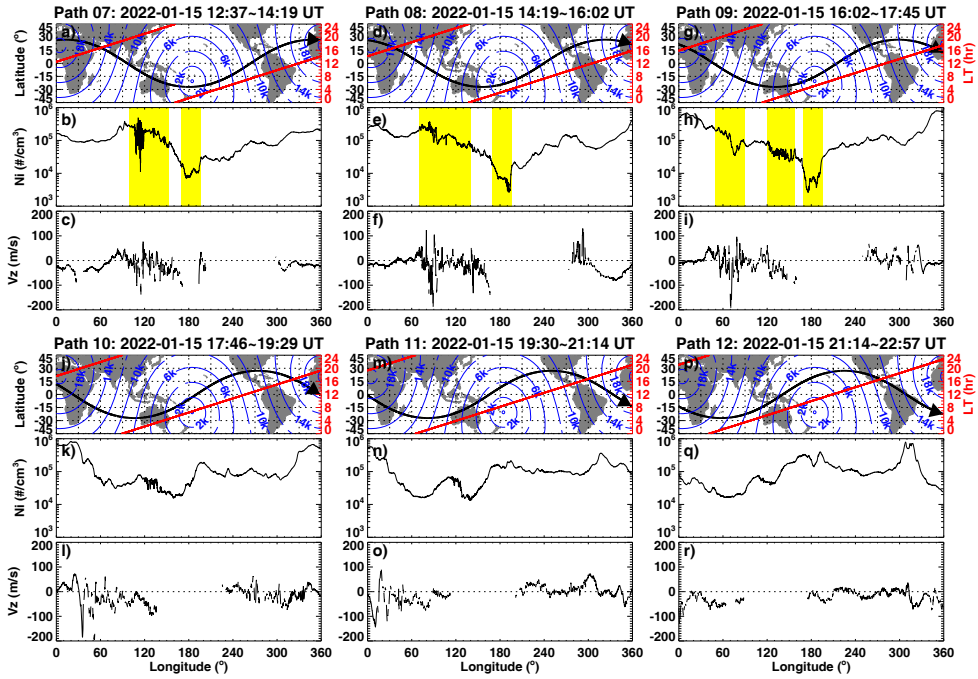


**Figure 7.** (a–r) The same as Figure 6, but for six following paths of ICON-IVM between 12:37–22:57 UT on 15 January 2022.

321 ICON-IVM in-situ measurements also observed significant co-volcanic and post-  
 322 volcanic ionospheric disturbances. Figure 6 shows ICON-IVM observation tracks and cor-  
 323 responding local time, ion density, and vertical drift results for six consecutive paths be-  
 324 tween 02:42–12:19 UT on 15 January 2022. In Path 01, the plasma density and verti-  
 325 cal drift variation were generally smooth over the Asia-Oceania sector with merely small  
 326 fluctuations before the Tonga volcanic eruption. Starting from Path 02, however, signif-  
 327 icant plasma density and drift disturbances were registered following the volcanic erup-  
 328 tion around epicenter and adjacent area. For example, at  $\sim 04:55$  UT in path 02, both  
 329 plasma density (Figure 6e) and vertical drift (Figure 6f) exhibited a sudden bump of “plasma  
 330 blob” near the volcanic eruption longitude around  $185^\circ$  ( $175^\circ$ W), although the latitu-  
 331 tudinal location of ICON observation was in the conjugate northern hemisphere at this mo-  
 332 ment around 4,000 km away from epic center. This would either require a fast propa-  
 333 gation mode (e.g., Rayleigh wave) of  $\sim 1700$ – $1800$  m/s that much larger than those known  
 334 air pressure acoustic wave modes indicated in Themens et al. (2022) and Zhang et al.  
 335 (2022); or an alternative explanation, as suggested by Lin et al. (2022) and also implied  
 336 from the vertical plasma drift spike, is that this was more like a conjugate disturbance  
 337 signature due to instantaneous magnetic field mapping effect of polarization electric field  
 338 induced by significant zonal wind perturbation due to volcano-induced AGWs. Future  
 339 modeling effort and data analysis is still needed to further verify the exact mechanism  
 340 of this fast conjugate response, which is beyond the scope of the current paper.

341 The most striking features shown by ICON-IVM are the strong plasma trough embed-  
 342 ded with plasma bubbles that appeared starting from Path 03. In particular, when  
 343 ICON was crossing the volcano eruption longitude between  $180$ – $195^\circ$ E around 06:40 UT  
 344 (Figure 6h, 19 LT), the in-situ plasma density experienced a drastic depletion of two or-

345 ders of magnitude, reaching as low as  $10^3 \text{ cm}^{-3}$  that highlighted by yellow shades. More-  
 346 over, noticeable EPBs were embedded within this huge equatorial plasma trough and were  
 347 associated with large vertical  $E \times B$  drift of 60–120 m/s (Figure 6i), representing enhanced  
 348 fountain effect near the local dusk after the volcanic eruption, which was favorable for  
 349 the amplification of Rayleigh-Taylor instability growth rate and development of plasma  
 350 irregularities (Kelley et al., 1976). Similarly, in Path 04, strong postsunset EPBs with  
 351 1–2 orders of magnitude depletion and large vertical  $E \times B$  drift of 60–120 m/s extended  
 352 westward between  $150\text{--}190^\circ$  longitudes around 08:15 UT. Moreover, in the following two  
 353 paths, the deep local plasma hole remained nearly stationary around the eruption cen-  
 354 ter. At the same time, significant postsunset EPBs in the Asian sector were gradually  
 355 separated from the local plasma hole but continuously developed at further westward  
 356 longitudes across  $130\text{--}170^\circ\text{E}$  around 10:00 UT in Path 05 and about  $110\text{--}150^\circ\text{E}$  around  
 357 11:40 UT in Path 06. Two important results can be derived from these observations: (1)  
 358 the horizontal size of the local plasma hole was quite noticeable, with an estimated ra-  
 359 dius of around  $10\text{--}15^\circ$  that consistent with the TEC results (Figure 2) and Swarm B es-  
 360 timation (Figure 4c); (2) the westward propagating phase speed of the continuously de-  
 361 veloped EPBs was estimated to be 310–350 m/s that generally agree with the Lamb waves  
 362 velocity (Themens et al., 2022; Zhang et al., 2022).

363 Figure 7 displays similar ICON-IVM results for the following six orbital paths be-  
 364 tween 12:37–22:57 UT on January 15. Local plasma hole and strong EPBs were still quite  
 365 considerable in Paths 07–09 as shown by yellow shades, which are consistent with Swarm  
 366 results. Starting from Path 10, this long-lasting local plasma hole seemed to be filled pos-  
 367 sibly by sunrise photo-ionization, as ICON passed the volcanic eruption longitudes in  
 368 local morning. EPBs in Asian sector were gradually diminished though still discernible  
 369 to some extent. One thing to note is that such a deep local plasma hole and strong EPBs  
 370 continued for more than 10 hours before completely subsidized, which is surprisingly unique  
 371 and will be further discussed in next section.

## 372 4 Discussion

### 373 4.1 Huge Local Ionospheric Plasma Hole and Oscillations

374 Beidou GEO TEC observing geometries provided a unique opportunity to contin-  
 375 uously observe and precisely evaluate the volcano-induced local ionosphere character-  
 376 istics using fixed IPPs. The most direct feature near the epicenter was a significant iono-  
 377 spheric hole with depletion magnitude of more than 10 TECU, forming by consecutive  
 378 cliff-like TEC drops. Such a deep ionospheric hole was also observed in the 2-D delta TEC  
 379 maps with 10+ TECU reduction and in ICON-IVM plasma density measurements with  
 380 1–2 orders of magnitude depletion. In particular, this ionospheric hole has a broad hor-  
 381 izontal size with an estimated radius of  $10\text{--}15^\circ$  and continued for several hours. Surpris-  
 382 ingly, such a huge depletion feature near epicenter was registered in ICON-IVM plasma  
 383 density profiles for more than 10 hours until local sunrise. Although a similar phenomenon  
 384 of a transient co-seismic ionospheric “hole” near the epicenter has been occasionally re-  
 385 ported before (e.g., Astafyeva et al., 2013; Kakinami et al., 2012; Tsugawa et al., 2011),  
 386 the magnitude, size, and duration of such a huge ionospheric hole after this volcanic erup-  
 387 tion are quite distinct. For example, the local depletion feature associated with the 2011  
 388 Japan Tohoku earthquake has a magnitude of 5–6 TECU reduction, a horizontal scale  
 389 size of 500 km, and a duration of 60 min (Saito et al., 2011), which are considerably less  
 390 than those of the Tonga volcanic eruption.

391 The underlying mechanism of such a huge plasma hole is still under debate. For  
 392 example, Kakinami et al. (2012) suggested that this is a tsunami-related depletion in-  
 393 duced by ionosphere descent and recombination enhancement through meter-scale sea  
 394 surface downwelling at the tsunami source region. However, Kamogawa et al. (2015) in-  
 395 dicated that this depletion could instead occur after a large inland earthquake. Astafyeva

et al. (2013) demonstrated that the depletion represents the rarefaction phase of shock-acoustic waves following large inland or undersea earthquake. Moreover, numerical simulation results given by Shinagawa et al. (2013) and Zettergren et al. (2017) collectively indicated that the TEC depletion was likely caused by strong expansion and upwelling in the thermosphere along with outward ionospheric plasma flow driven by impulsive non-linear shock-acoustic wave pulses. This latter mechanism helps explain our direct observational evidence in this Tonga event: the local TEC depletion was composed of cascading decreases that corresponding to different shock-acoustic wave impulses. In addition, Astafyeva et al. (2022) also observed this plasma hole and indicated that the Tonga volcanic eruption from shallow underwater should generate stronger shock waves with large amplitude and prolonged rarefaction phase than those from inland earthquake. This helps explain the unprecedented magnitude and size of the ionospheric hole. Another thing worth noting is that this local plasma hole was established near local dusk with a long-lasting duration that registered in ICON-IVM ion density profiles (Figures 6 and 7) for more than 10 hours until local sunrise, primarily due to shortage of nighttime photoionization source with low background density level, as well as lack of field-aligned plasmaspheric refilling due to smaller dip angle in the low-latitude region.

Besides the large ionospheric hole, several acoustic-gravity oscillation modes with different propagation velocities were identified. The fast modes with 1050 m/s and 760 m/s, arising from different excitation conditions, fall within the sound speed range at ionospheric heights and are comparable to prior studies (e.g., Calais et al., 1998; Heki & Ping, 2005; Heki, 2006; Otsuka et al., 2006). These modes are considered to be caused by acoustic pressure waves generated from the sea surface at the epicenter (Astafyeva, 2019; Chen et al., 2011; Tsugawa et al., 2011). The subsequent medium-speed modes between 300–500 m/s range could be associated with lower-frequency infrasonic and/or gravity parts of AGWs, which propagated to at least 3500 km away as deduced from Figure 1h. The ionospheric disturbances also included a slower propagation mode with speeds of 180–250 m/s, due to gravity waves triggered by volcano and/or tsunami–atmosphere–ionosphere coupling processes (e.g., Artru et al., 2005; Azeem et al., 2017; Huba et al., 2015; Savastano et al., 2017; Meng et al., 2018).

## 4.2 Strong Post-volcanic EPBs

The most significant discovery of this study is the presence of strong and long-lasting post-volcanic EPBs that continuously developed across the Asia-Oceania area on January 15, covering a wide longitudinal range for more than  $140^\circ$  with duration  $\geq 12$  hours and  $N_e$  decrease of 2–3 orders of magnitude at Swarm/ICON altitude between 450–575 km. In contrast, EPB activities on the day before and after the volcano eruption were much weaker as shown in Figure 4. It is known that EPBs are large-scale plasma density depletions that usually form in the postsunset bottomside F region at the equatorial and low-latitude ionosphere, under favorable conditions of prereversal enhancement (PRE) and increased Rayleigh-Taylor instability growth rate with steep vertical density gradients after the decay of E region (e.g., Abdu, 2005; Aa et al., 2019; Karan et al., 2020). Although co-seismic and co-volcanic AGWs and associated ionospheric oscillations have been widely reported, to the best of our knowledge, such widespread and long-lasting post-volcanic EPB features have never been reported before, especially considering that the seasonal behavior of EPBs' occurrence over Asian and Pacific sector is typically quite low around January that derived from climatology studies (e.g., Burke et al., 2004; Aa, Zou, & Liu, 2020; Kil et al., 2009). The mechanism of these anomalous post-volcanic EPBs needs detailed discussion.

The first thing to consider is magnetospheric driving forces from above since this volcano eruption happened during the recovery phase of a moderate geomagnetic storm. Depending on storm phases and local time sectors, the EPBs occurrence can be enhanced or inhibited primarily via modified equatorial electrodynamic effects caused by the pen-

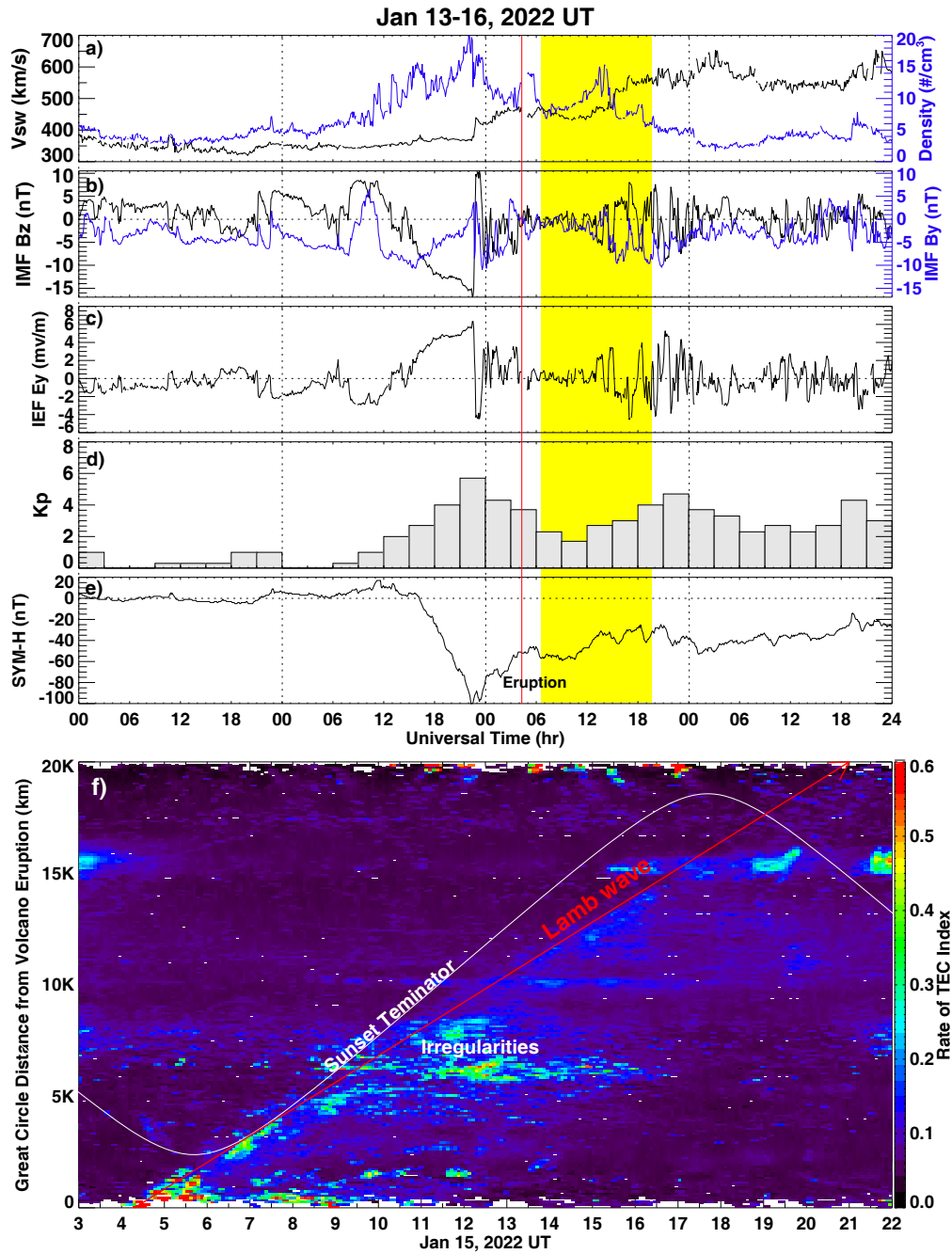


**Figure 8.** Temporal variation of (a) Solar wind speed and proton density, (b) Interplanetary magnetic field (IMF) B<sub>y</sub> and B<sub>z</sub>, (c) interplanetary electric field (IEF) B<sub>y</sub>, (d) K<sub>p</sub> index, and (e) Longitudinally symmetric index (SYM-H) during January 13-16, 2022. The volcano eruption time was marked with a vertical red line. The yellow shade marks the approximate time period for EPBs observations. (f) UT-distance variation of ROTI values. The Lamb wave propagation trend (red line) and equatorial sunset terminator (white line) was also marked.

448 etration electric field (PEF) due to suddenly varying magnetospheric convection, and/or  
 449 disturbance dynamo electric field (DDEF) due to changes in global thermosphere cir-  
 450 culation. (1) Storm enhances EPBs. This usually occurs in the storm main phase when  
 451 PEF has the same eastward polarity as dusktime PRE. This combination leads to in-  
 452 creased upward equatorial plasma drift and the enhanced postsunset rise (PSSR) of F-  
 453 layer height, which provides favorable conditions to enlarge the growth rate of Rayleigh-  
 454 Taylor instability (e.g., Aa et al., 2019; Cherniak & Zakharenkova, 2016; Jin et al., 2018;  
 455 Tulasi Ram et al., 2008). In some rare cases, nighttime DDEF can sometimes excite atyp-  
 456 ical predawn EPBs (Zakharenkova et al., 2019). (2) Storm inhibits EPBs. This usually  
 457 occurs in the storm recovery phase when DDEF has been built up with a westward po-  
 458 larity in the daytime through local dusk. The modified westward equatorial zonal elec-  
 459 tric field leads to downward plasma drift and lowering of the F-layer, causing suppres-  
 460 sion of postsunset EPBs (e.g., Carter et al., 2016; Li et al., 2009).

461 For this event, Figures 8a–8e show temporal variation of interplanetary and geo-  
 462 magnetic parameters between January 13–16, 2022. On January 14, following a coro-  
 463 nal mass ejection (CME) arrival, the Interplanetary Magnetic Field (IMF)  $B_z$  (Figure 8b)  
 464 rotated to a sustained negative direction after 15 UT, reaching a minimum value of -17 nT  
 465 at 22:25 UT and quickly flipped northward. This indicates the existence of large PEF  
 466 at the end of January 14 as also shown in interplanetary electric field (IEF)  $E_y$  (Figure 8c).  
 467 The Kp index reached 6 between 21–24 UT and the longitudinally symmetric index (SYM-  
 468 H) reached a minimum value of -100 nT at 22:25 UT, which registered this storm as a  
 469 moderate storm. The large PEF existed around 16–23 UT on January 14, the previous  
 470 day of the volcano eruption. During this period, the Asia-Oceania sector was rotating  
 471 from local midnight to morning with westward PEF, which inhibited EPBs occurrence  
 472 therein as can be seen from background dotted lines in Swarm  $N_e$  in Figure 4. However,  
 473 we emphasize that the observed significant EPBs in the Asia-Oceania sector were mainly  
 474 around 06–18 UT on January 15, about 12 hours after this large PEF. As can be seen,  
 475 the IMF  $B_z$  and IEF has already subsided and exhibited merely small perturbations at  
 476 least between 04–15 UT on January 15 before detected EPBs. Thus, it is hard to prove  
 477 that the large PEF, which inhibited EPBs in Asian-Oceania sector on January 14, would  
 478 have continued for over 12 hours and caused resurgent EPBs on the second day, since  
 479 the penetration effect is typically prompt and short-lived in a couple of hours. There were  
 480 some fluctuations in IMF and IEF since 15 UT on January 15 due to the arrival of coro-  
 481 nal hole high-speed stream, which may provide intermittent PEF to maintain plasma bub-  
 482 bles. However, the initial equatorial trough and plasma bubbles occurred much earlier  
 483 around 06–07 UT as shown by ICON-IVM results. Moreover, January 16 also registered  
 484 moderate IMF  $B_z$  and IEF  $E_y$  fluctuations in the latter half of the day, suggesting the  
 485 existence of intermittent PEF similar to that of the volcano eruption day, yet the EPBs  
 486 activity was much weaker on January 16 as can be seen from dashed lines in Figure 4.  
 487 These collectively indicate that the intermittent PEF was unlikely the dominant driver  
 488 of significant EPBs over the Asia-Oceania sector on volcano eruption day.

489 We next discuss the potential DDEF effect. The observed EPBs occurred in the  
 490 storm recovery phase, and it is possible that DDEF may have been built up around low  
 491 latitudes. However, it is known that the polarity of DDEF is typically westward in the  
 492 daytime through local dusk (M. Blanc & Richmond, 1980), which normally causes storm-  
 493 time inhibition of EPBs in the postsunset sector via downward  $E \times B$  drift to reduce the  
 494 instability growth rate (e.g., Carter et al., 2016; Li et al., 2009). In this study, signifi-  
 495 cant EPBs occurred in the postsunset hours. Thus, we deduce that the storm-time DDEF  
 496 is unlikely the primary cause of this event. Moreover, the ICON-IVM drift results in Fig-  
 497 ures 6f and 6i showed that the vertical plasma drift exhibited a sudden enhancement right  
 498 around the eruption longitude. The storm-induced penetration or disturbance dynamo  
 499 electric fields are not expected to have such a sharp longitudinal distinction but usually  
 500 exhibit a wide longitudinal coverage with the same polarity during the day/night. Last  
 501 but not least, recent studies given by Harding et al. (2022) and Le et al. (2022) have in-

502 investigated equatorial electrojet activities for this same event using ICON/MIGHTI neu-  
 503 tral wind measurements, Swarm field-line current data, and ground-based magnetome-  
 504 ter data, indicating that the penetration and disturbance dynamo electric field from this  
 505 geomagnetic storm had minimal impact on the equatorial electric field perturbation.

506 Therefore, besides the storm effect, we next discuss lower atmosphere forces after  
 507 the volcano eruption. Figure 8f shows a GNSS ROTI figure as a function of universal  
 508 time and great-circle distance from volcano eruption location. This time-distance plot  
 509 was constructed to compensate for the uneven GNSS data distribution by binning all  
 510 available ROTI measurements in terms of the universal time and great-circle distance  
 511 from the volcano eruption site. Note that high-latitude ROTI data above  $65^\circ$  geomag-  
 512 netic latitude were excluded to eliminate space weather impacts as much as possible. This  
 513 time-distance figure would allow us to better identify and trace the volcano-induced dis-  
 514 turbances propagation signature. As can be seen, volcano-induced ionospheric distur-  
 515 bances travelled globally at least 16,000 km away from the epicenter. By calculating the  
 516 slope of the fitted line along the discernible boundary, the global propagation velocity  
 517 of ionospheric ROTI disturbances is about  $315 \pm 15$  m/s, consistent with the globally prop-  
 518 agating nature of less-attenuating atmospheric Lamb waves from historical and recent  
 519 corroborations (Bretherton, 1969; Lindzen & Blake, 1972; Themens et al., 2022; Zhang  
 520 et al., 2022). Despite Lamb waves are normally concentrated within a few scale heights  
 521 in the troposphere/stratosphere, their energy can tunnel into the thermosphere via acoustic-  
 522 gravity resonance at certain frequencies and thus can further cause ionospheric distur-  
 523 bances (Nishida et al., 2014). Thus, we observed moderate-to-high ROTI values ( $>0.25$ )  
 524 representing strong ionospheric irregularities that predominantly occurred between 3000–  
 525 10000 km range around 07–16 UT, mainly contributed by Asia-Oceania observations,  
 526 following the continuous passage of equatorial sunset terminator and volcano-induced  
 527 Lamb waves.

528 This coincident terminator/wave passage and irregularities suggest that acoustic-  
 529 gravity resonance and coupling with Lamb waves may explain the occurrence of such strong  
 530 EPBs. It is known that the connection between gravity waves and plasma bubbles have  
 531 been widely studied using both observations and numerical simulations. For example,  
 532 Hysell et al. (1990) found gravity wave modulations were related to radar irregularity  
 533 plume formation over Jicamarca; Rottger (1981) indicated that gravity waves from con-  
 534 vective thunderstorm have a reasonable impact on equatorial spread-F irregularities; Singh  
 535 et al. (1997) indicated that plasma bubble signatures can be developed from wavy ion  
 536 density structures in the bottomside F layer; Takahashi et al. (2009) and Fritts et al. (2008)  
 537 observed simultaneous appearance of periodic EPBs and upward propagating gravity waves  
 538 reaching thermospheric height during the Spread F Experiment. C.-S. Huang and Kel-  
 539 ley (1996) simulated the non-linear evolution of Spread-F irregularities induced by the  
 540 zonally propagating gravity waves. Numerical simulations given by Krall et al. (2013)  
 541 and Tsunoda (2010) investigated the seeding role of Spread-F irregularity due to plane  
 542 and circular gravity waves, respectively. Despite these interesting studies, our analysis  
 543 of this unique natural hazard event indicates a novel linkage between the volcanic erup-  
 544 tion and plasma bubbles that provides further evidence to help verify and understand  
 545 the underlying mechanisms.

546 In particular, the development of plasma bubbles could be attributed to volcano-  
 547 induced AGWs via the following three mechanisms:

548 (1) Direct seeding mechanism. The wave disturbances propagating upward at slant  
 549 angles could produce needed perturbation winds, providing precursor modulations in the  
 550 electron density and/or polarization electric field to initiate the instability growth (e.g.,  
 551 C.-S. Huang & Kelley, 1996; Krall et al., 2013; Huba & Liu, 2020; Retterer & Roddy,  
 552 2014; Tsunoda, 2010). In particular, the meridional wind perturbations of gravity wave  
 553 could produce plasma density modulations via dynamic effect; the zonal and vertical wind  
 554 perturbations across geomagnetic field lines can generate polarization electric field (Abdu

555 et al., 2009). Both of which contribute to the instability growth of EPBs development.  
 556 Using ICON thermospheric wind measurements, Harding et al. (2022) found that both  
 557 zonal and meridional winds exhibited strong oscillations as large as  $\pm 200$  m/s follow-  
 558 ing the passage of volcano-induced Lamb waves. This could provide initial seed pertur-  
 559 bations that lead to the development of EPBs.

560 (2) Destabilize bottomside ionospheric gradient. The gravity wave amplitude is known  
 561 to increase exponentially with respect to altitude due to decreasing atmospheric density,  
 562 which could form large-scale wave structures in the bottomside F region that undulate  
 563 F layer heights to elevate and destabilize bottomside density gradients (Abdu et al., 2009;  
 564 Tsunoda et al., 2011). Several studies have thus indicated that EPBs could be developed  
 565 at the crests of large-scale wave structures and exhibited periodic longitudinal distribu-  
 566 tions with inter-bubble distances of several hundred kilometers (e.g., Aa, Zou, Eastes,  
 567 et al., 2020; Das et al., 2020; Makela et al., 2010; Takahashi et al., 2015). For this vol-  
 568 canic eruption event, the observed EPBs also exhibited quasi-periodic longitudinal struc-  
 569 tures as shown in TEC keogram (Figure 4c) and in ICON-IVM plasma density profiles  
 570 (Figures 6k, 6n, and 6q), which are consistent with the horizontal wavelength of several  
 571 hundred kilometers for the global propagating TIDs related to Lamb waves in both near-  
 572 field and far-field (Zhang et al., 2022). This further demonstrates the existence and in-  
 573 fluence of Lamb wave-induced gravity waves in triggering EPBs.

574 (3) Enhancement of PRE and postsunset rise of equatorial F-layer. Gravity waves  
 575 can be a necessary factor to trigger initial plasma perturbations but may not always be  
 576 a sufficient source leading to plasma bubbles (Huba & Liu, 2020). The background iono-  
 577 spheric condition, especially the equatorial vertical  $E \times B$  drift, is a key factor that di-  
 578 rectly influences the Rayleigh-Taylor instability growth rate (Sultan, 1996). It is known  
 579 that large eastward thermospheric wind near the equatorial dusk region is responsible  
 580 for the PRE via F-region dynamo effect (Eccles et al., 2015; Rishbeth, 1971). The PRE  
 581 peak intensity could be enhanced by in-phase superposition of eastward perturbation wind  
 582 due to AGWs and the background zonal wind (Abdu et al., 2009; Kudeki et al., 2007).  
 583 Some recent studies showed that this volcanic eruption caused extreme thermospheric  
 584 zonal winds oscillation with the maximum eastward component reaching 200 m/s together  
 585 with strong equatorial electrojet following the passage of volcano-induced Lamb waves  
 586 (Harding et al., 2022; Le et al., 2022). In comparison, our study of the ICON-IVM ver-  
 587 tical drift measurements clearly demonstrates that the dusktime PRE near epicenter lon-  
 588 gitude was indeed largely enhanced to 60–120 m/s (Figures 6f, 6i, and 6l) following the  
 589 volcanic eruption. Moreover, the broad equatorial plasma depletion with 20–25° latitu-  
 590 dinal width in Swarm B Ne profile of Path 02 (Figure 4b) also implied that the ionospheric  
 591 height near the epicenter longitude could be significantly uplifted so that satellite was  
 592 likely flying below the F2 region peak height to encounter low-density region. Further-  
 593 more, Figure 9 shows an equatorial ionosonde measurements of Ne profile and F2-layer  
 594 peak height (hmF2) at GUAM between January 13–16, 2022. As can be seen, GUAM  
 595 hmF2 exhibited a strong postsunset rise (PSSR) to 440 km at  $\sim 09$  UT on January 15  
 596 around the anticipated arrival time of volcano-induced atmospheric Lamb waves as marked  
 597 by a white arrow. This postsunset rise of F-layer was 60–80 km considerably larger than  
 598 that of other reference days. The IMF Bz/By and IEF had mere limited variations around  
 599 this time, indicating weak penetration electric field effect. Such a large enhancement of  
 600 PRE magnitude and postsunset rise of equatorial ionospheric F-layer led to increased  
 601 R-T instability growth rate and thus contributed to vigorous EPBs that were shown in  
 602 ICON-IVM and Swarm in-situ measurements. Moreover, Figure 8f displays the time-distance  
 603 variation of ROTI values with the equatorial sunset terminator and Lamb wave prop-  
 604 agation trend being marked. As can be seen, the equatorial dusk terminator and Lamb  
 605 wave swept over the wide Asia-Oceania area almost simultaneously or consecutively since  
 606  $\sim 06:30$  UT, which provides a favorable background condition with increased PRE and  
 607 Rayleigh-Taylor instability growth rate under the right timing of direct AGWs seeding  
 608 induced by the volcanic eruption. The longitudinal extension of these strong EPBs was

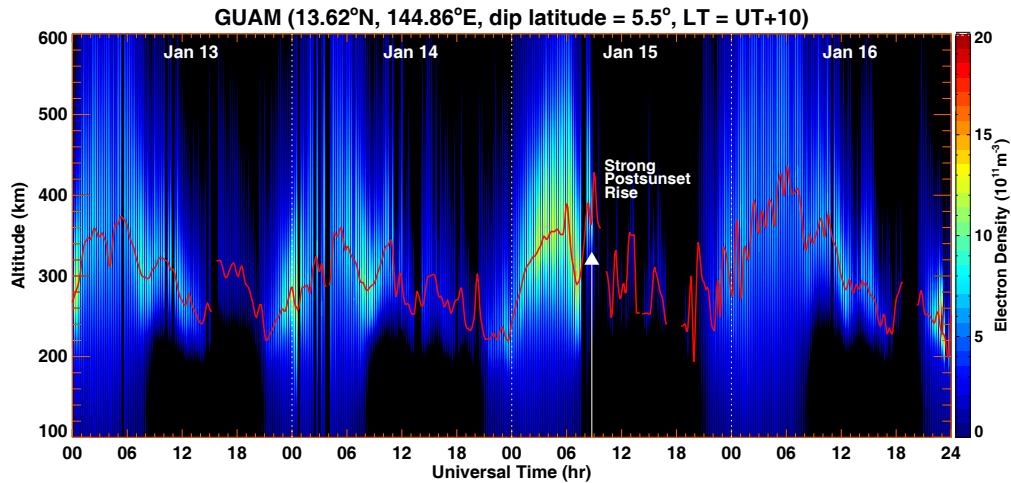


**Figure 9.** GUAM ionosonde measurements of electron density profiles and F2-layer peak height (hmF2) during January 13-16, 2022. The white arrow marks the anticipated arrival time of atmospheric Lamb waves that associated with strong postsunset rise of equatorial F layer around 09 UT on January 15.

609 over  $140^\circ$ , which is slightly smaller but comparable to the longitudinal extension of volcano-  
 610 induced TIDs (Zhang et al., 2022). This provides further evidence to support the con-  
 611 nection between these strong EPBs and volcano-induced AGWs.

612 In aggregate, these volcano-related factors could work together to catalyze and am-  
 613 plify initial plasma density perturbations as well as to contribute to increased PRE/PSSR  
 614 and Rayleigh-Taylor instability growth rate, which effectively facilitated the development  
 615 of pronounced and extensive EPBs over wide Asia-Oceania longitudes following the con-  
 616 secutive passage of sunset terminator and atmospheric Lamb waves. The storm-modified  
 617 electric field might provide a partial contribution. Future simulation work is needed to  
 618 investigate further this significant EPB event with surface-to-ionosphere connections, which  
 619 is beyond the scope of the current observation study.

## 620 5 Conclusions

621 Local and global ionospheric disturbances associated with the 2022 Tonga volcano  
 622 eruption were studied using both ground-based and space-borne observations, includ-  
 623 ing Beidou GEO TEC from fixed IPPs, multi-GNSS ROTI data, Swarm and ICON in-  
 624 situ measurements, as well as ionosonde measurements. The main results and findings  
 625 are as follows:

626 1. The volcano eruption resulted in a significant local ionospheric hole of more than  
 627 10 TECU near the epicenter that consisted of cascading TEC decreases and oscillations.  
 628 The horizontal radius of this plasma hole was estimated to be around  $10\text{--}15^\circ$ . This could  
 629 be explained by strong thermosphere expansion and large ionosphere outward flow driven  
 630 by consecutive intense co-volcanic shock-acoustic wave impulses. This plasma hole sig-  
 631 nature persisted for more than 10 hours in ICON-IVM plasma density profiles until lo-

632 cal sunrise, likely due to a shortage of nighttime photo-ionization sources with low back-  
 633 ground density levels.

634 2. We observed both local and distant ionospheric large-amplitude disturbances  
 635 due to various volcano-induced AGW modes with different phase velocities, including  
 636 fast acoustic modes of  $\sim 1050$  m/s and  $\sim 760$  m/s, infrasonic mode of  $\sim 460$  m/s, atmo-  
 637 spheric Lamb waves mode of  $\sim 315$  m/s, and tsunami-gravity modes of  $\sim 180$ – $250$  m/s.  
 638 The atmospheric Lamb waves mode exhibited the most distinct long-distance travelling  
 639 feature reaching at least 16,000 km away from the epicenter, causing significant global-  
 640 scale ionospheric disturbances via acoustic-gravity resonance and wave coupling.

641 3. For the first time, we observed pronounced equatorial plasma trough and pro-  
 642 longed post-volcanic evening plasma bubbles over the Asia-Oceania area, following the  
 643 volcano-eruption that associated with enhanced dusktime upward plasma drifts of 60–  
 644 120 m/s. The observed plasma bubbles continuously developed across a wide longitu-  
 645 dinal area at an approximate Lamb wave velocity over  $140^\circ$  and lasted around 12 hours,  
 646 with plasma density decreased by 2–3 orders of magnitude at Swarm/ICON altitude be-  
 647 tween 450–575 km. Given that the dusk terminator and westbound propagating Lamb  
 648 waves swept over the Asia-Oceania area consecutively, significant plasma bubbles were  
 649 likely seeded by gravity resonance and coupling with less-damped Lamb waves, under  
 650 the right timing with favorable background conditions of largely increased PRE and post-  
 651 sunset rise of equatorial F-layer to effectively amplify the Rayleigh-Taylor instability growth  
 652 rate via volcano-induced AGWs. The storm-modified electric field could also play a sec-  
 653 ondary role though its specific contribution needs future investigation.

## 654 Data Availability Statement

655 GNSS TEC data products are provided through the Madrigal distributed data sys-  
 656 tem at (<http://cedar.openmadrigal.org/>) by MIT. Swarm data are provide by Eu-  
 657 ropean Space Agency (<https://swarm-diss.eo.esa.int/>). The ICON data can be ac-  
 658 cessed at (<https://icon.ssl.berkeley.edu/Data>). The cloud brightness temperature  
 659 data are provided by NASA Goddard Earth Sciences Data and Information Services Cen-  
 660 tral ([https://disc.gsfc.nasa.gov/datasets/GPM\\_MERGIR\\_1/summary](https://disc.gsfc.nasa.gov/datasets/GPM_MERGIR_1/summary)). The solar wind  
 661 and geophysical parameters data is acquired from NASA/GSFC's Space Physics Data  
 662 Facility's OMNIWeb service (<https://cdaweb.gsfc.nasa.gov/>) and Kyoto world data  
 663 center for Geomagnetism (<http://wdc.kugi.kyoto-u.ac.jp/>).

## 664 Acknowledgments

665 GNSS TEC data are part of the U.S. NSF's Millstone Hill Geospace Facility program  
 666 under AGS-1952737 with MIT. We acknowledge NSF awards AGS-2033787 and PHY-  
 667 2028125, NASA support 80NSSC22K0171, 80NSSC21K1310, 80NSSC21K1775, and 80NSSC19K0834,  
 668 AFOSR MURI Project FA9559-16-1-0364, and ONR Grant N00014-17-1-2186. Data for  
 669 TEC processing is provided from the following organizations: UNAVCO, SOPAC, IGN  
 670 (France), IGS, CDDIS, NGS, IBGE (Brazil), RAMSAC (Argentina), CORS (Panama),  
 671 Arecibo Observatory, LISN, Topcon, CHAIN (Canada), CRS (Italy), SONEL, RENAG  
 672 (New Zealand), GNSS Reference Networks, Finnish Meteorological Institute, and SWE-  
 673 POS.

674

**References**

675

Aa, E., Zou, S., Eastes, R., Karan, D. K., Zhang, S.-R., Erickson, P. J., & Coster, A. J. (2020, January). Coordinated Ground-Based and Space-Based Observations of Equatorial Plasma Bubbles. *Journal of Geophysical Research (Space Physics)*, *125*(1), e27569. doi: 10.1029/2019JA027569

677

678

679

Aa, E., Zou, S., & Liu, S. (2020, April). Statistical Analysis of Equatorial Plasma Irregularities Retrieved From Swarm 2013-2019 Observations. *Journal of Geophysical Research: Space Physics*, *125*(4), e27022. doi: 10.1029/2019JA027022

681

682

683

Aa, E., Zou, S., Ridley, A., Zhang, S., Coster, A. J., Erickson, P. J., ... Ren, J. (2019, February). Merging of Storm Time Midlatitude Traveling Ionospheric Disturbances and Equatorial Plasma Bubbles. *Space Weather*, *17*(2), 285-298. doi: 10.1029/2018SW002101

684

685

686

Abdu, M. A. (2005). Equatorial ionosphere thermosphere system: Electrodynamics and irregularities. *Adv. Space Res.*, *35*, 771-787. doi: 10.1016/j.asr.2005.03.150

687

688

689

Abdu, M. A., Alam Kherani, E., Batista, I. S., de Paula, E. R., Fritts, D. C., & Sobral, J. H. A. (2009, July). Gravity wave initiation of equatorial spread F/plasma bubble irregularities based on observational data from the SpreadFEx campaign. *Annales Geophysicae*, *27*(7), 2607-2622. doi: 10.5194/angeo-27-2607-2009

690

691

692

Afraimovich, E. L., Feng, D., Kiryushkin, V. V., & Astafyeva, E. I. (2010, November). Near-field TEC response to the main shock of the 2008 Wenchuan earthquake. *Earth, Planets and Space*, *62*(11), 899-904. doi: 10.5047/eps.2009.07.002

693

694

695

Artru, J., Ducic, V., Kanamori, H., Lognonné, P., & Murakami, M. (2005, March). Ionospheric detection of gravity waves induced by tsunamis. *Geophysical Journal International*, *160*(3), 840-848. doi: 10.1111/j.1365-246X.2005.02552.x

696

697

698

Artru, J., Farges, T., & Lognonné, P. (2004, September). Acoustic waves generated from seismic surface waves: propagation properties determined from Doppler sounding observations and normal-mode modelling. *Geophysical Journal International*, *158*(3), 1067-1077. doi: 10.1111/j.1365-246X.2004.02377.x

699

700

701

Astafyeva, E. (2019, December). Ionospheric Detection of Natural Hazards. *Reviews of Geophysics*, *57*(4), 1265-1288. doi: 10.1029/2019RG000668

702

703

704

Astafyeva, E., Maletckii, B., Mikesell, T. D., Munaibari, E., Ravenelli, M., Coisson, P., ... Rolland, L. (2022). The 15 January 2022 Hunga Tonga eruption history as inferred from ionospheric observations. *Earth and Space Science Open Archive*. doi: 10.1002/essoar.10511226.1

705

706

707

Astafyeva, E., Shalimov, S., Olshanskaya, E., & Lognonné, P. (2013, May). Ionospheric response to earthquakes of different magnitudes: Larger quakes perturb the ionosphere stronger and longer. *Geophysical Research Letters*, *40*(9), 1675-1681. doi: 10.1002/grl.50398

708

709

710

Azeem, I., Vadas, S. L., Crowley, G., & Makela, J. J. (2017, March). Traveling ionospheric disturbances over the United States induced by gravity waves from the 2011 Tohoku tsunami and comparison with gravity wave dissipative theory. *Journal of Geophysical Research: Space Physics*, *122*(3), 3430-3447. doi: 10.1002/2016JA023659

711

712

713

Blanc, E. (1985, December). Observations in the upper atmosphere of infrasonic waves from natural or artificial sources - A summary. *Annales Geophysicae*, *3*, 673-687.

714

715

716

Blanc, M., & Richmond, A. D. (1980, April). The ionospheric disturbance dynamo. *Journal of Geophysical Research*, *85*(A4), 1669-1686. doi: 10.1029/JA085iA04p01669

717

718

719

Bretherton, F. P. (1969, October). Lamb waves in a nearly isothermal atmosphere. *Quarterly Journal of the Royal Meteorological Society*, *95*(406), 754-757. doi:

720

721

722

723

724

725

726

727

728

- 729 10.1002/qj.49709540608  
730 Burke, W. J., Gentile, L. C., Huang, C. Y., Valladares, C. E., & Su, S. Y. (2004,  
731 December). Longitudinal variability of equatorial plasma bubbles observed by  
732 DMSP and ROCSAT-1. *Journal of Geophysical Research*, *109*(A12), A12301.  
733 doi: 10.1029/2004JA010583
- 734 Cahyadi, M. N., & Heki, K. (2013, April). Ionospheric disturbances of the 2007  
735 Bengkulu and the 2005 Nias earthquakes, Sumatra, observed with a regional  
736 GPS network. *Journal of Geophysical Research: Space Physics*, *118*(4), 1777-  
737 1787. doi: 10.1002/jgra.50208
- 738 Calais, E., Bernard Minster, J., Hofton, M., & Hedlin, M. (1998, January). Iono-  
739 spheric signature of surface mine blasts from Global Positioning System  
740 measurements. *Geophysical Journal International*, *132*(1), 191-202. doi:  
741 10.1046/j.1365-246X.1998.00438.x
- 742 Carter, B. A., Yizengaw, E., Pradipta, R., Retterer, J. M., Groves, K., Valladares,  
743 C., ... Zhang, K. (2016, January). Global equatorial plasma bubble occurrence  
744 during the 2015 St. Patrick's Day storm. *J. Geophys. Res. Space Physics*, *121*,  
745 894-905. doi: 10.1002/2015JA022194
- 746 Chen, C. H., Saito, A., Lin, C. H., Liu, J. Y., Tsai, H. F., Tsugawa, T., ... Mat-  
747 sumura, M. (2011, July). Long-distance propagation of ionospheric disturbance  
748 generated by the 2011 off the Pacific coast of Tohoku Earthquake. *Earth,*  
749 *Planets and Space*, *63*(7), 881-884. doi: 10.5047/eps.2011.06.026
- 750 Cherniak, I., Krankowski, A., & Zakharenkova, I. (2014, August). Observation of  
751 the ionospheric irregularities over the Northern Hemisphere: Methodology and  
752 service. *Radio Sci.*, *49*, 653-662. doi: 10.1002/2014RS005433
- 753 Cherniak, I., & Zakharenkova, I. (2016, November). First observations of super  
754 plasma bubbles in Europe. *Geophysical Research Letters*, *43*(21), 11,137-  
755 11,145. doi: 10.1002/2016GL071421
- 756 Chou, M.-Y., Cherniak, I., Lin, C. C. H., & Pedatella, N. M. (2020, April).  
757 The Persistent Ionospheric Responses Over Japan After the Impact of the  
758 2011 Tohoku Earthquake. *Space Weather*, *18*(4), e02302. doi: 10.1029/  
759 2019SW002302
- 760 Das, S. K., Patra, A. K., Kherani, E. A., Chaitanya, P. P., & Niranjana, K. (2020,  
761 August). Relationship Between Presunset Wave Structures and Inter-  
762 bubble Spacing: The Seeding Perspective of Equatorial Plasma Bubble.  
763 *Journal of Geophysical Research: Space Physics*, *125*(8), e28122. doi:  
764 10.1029/2020JA028122
- 765 Dautermann, T., Calais, E., Lognonné, P., & Mattioli, G. S. (2009, December).  
766 Lithosphere-atmosphere-ionosphere coupling after the 2003 explosive eruption  
767 of the Soufriere Hills Volcano, Montserrat. *Geophysical Journal International*,  
768 *179*(3), 1537-1546. doi: 10.1111/j.1365-246X.2009.04390.x
- 769 Dautermann, T., Calais, E., & Mattioli, G. S. (2009, February). Global Po-  
770 sitioning System detection and energy estimation of the ionospheric wave  
771 caused by the 13 July 2003 explosion of the Soufrière Hills Volcano, Montser-  
772 rat. *Journal of Geophysical Research: Solid Earth*, *114*(B2), B02202. doi:  
773 10.1029/2008JB005722
- 774 Duncombe, J. (2022). The surprising reach of Tonga's giant atmospheric waves.  
775 *Eos: AGU Science News*, *103*. Retrieved from [https://doi.org/10.1029/  
776 2022E0220050](https://doi.org/10.1029/2022E0220050)
- 777 Eccles, J. V., St. Maurice, J. P., & Schunk, R. W. (2015, June). Mechanisms  
778 underlying the prereversal enhancement of the vertical plasma drift in the low-  
779 latitude ionosphere. *Journal of Geophysical Research: Space Physics*, *120*(6),  
780 4950-4970. doi: 10.1002/2014JA020664
- 781 Foster, J. C., & Rich, F. J. (1998, November). Prompt midlatitude electric field  
782 effects during severe geomagnetic storms. *Journal of Geophysical Research*,  
783 *103*(A11), 26367-26372. doi: 10.1029/97JA03057

- 784 Friis-Christensen, E., Lühr, H., Knudsen, D., & Haagmans, R. (2008, January).  
 785 Swarm-An Earth Observation Mission investigating Geospace. *Advances in*  
 786 *Space Research*, *41*(1), 210-216. doi: 10.1016/j.asr.2006.10.008
- 787 Fritts, D. C., Vadas, S. L., Riggins, D. M., Abdu, M. A., Batista, I. S., Taka-  
 788 hashi, H., ... Taylor, M. J. (2008, October). Gravity wave and tidal in-  
 789 fluences on equatorial spread F based on observations during the Spread F  
 790 Experiment (SpreadFEx). *Annales Geophysicae*, *26*(11), 3235-3252. doi:  
 791 10.5194/angeo-26-3235-2008
- 792 Hao, Y.-Q., Xiao, Z., & Zhang, D.-H. (2006, July). Responses of the Ionosphere  
 793 to the Great Sumatra Earthquake and Volcanic Eruption of Pinatubo. *Chinese*  
 794 *Physics Letters*, *23*(7), 1955-1957. doi: 10.1088/0256-307X/23/7/082
- 795 Harding, B. J., Wu, Y.-J. J., Alken, P., Yamazaki, Y., Triplett, C. C., Immel, T. J.,  
 796 ... Xiong, C. (2022). Impacts of the January 2022 Tonga volcanic erup-  
 797 tion on the ionospheric dynamo: ICON-MIGHTI and Swarm observations of  
 798 extreme neutral winds and currents. *Geophysical Research Letters*, *49*(9),  
 799 e2022GL098577. doi: 10.1029/2022GL098577
- 800 Heelis, R. A., Stoneback, R. A., Perdue, M. D., Depew, M. D., Morgan, W. A.,  
 801 Mankey, M. W., ... Holt, B. J. (2017, October). Ion Velocity Measurements  
 802 for the Ionospheric Connections Explorer. *Space Science Review*, *212*(1-2),  
 803 615-629. doi: 10.1007/s11214-017-0383-3
- 804 Heki, K. (2006, July). Explosion energy of the 2004 eruption of the Asama Vol-  
 805 cano, central Japan, inferred from ionospheric disturbances. *Geophysical Re-*  
 806 *search Letters*, *33*(14), L14303. doi: 10.1029/2006GL026249
- 807 Heki, K., & Ping, J. (2005, August). Directivity and apparent velocity of the co-  
 808 seismic ionospheric disturbances observed with a dense GPS array. *Earth and*  
 809 *Planetary Science Letters*, *236*(3-4), 845-855. doi: 10.1016/j.epsl.2005.06.010
- 810 Hines, C. O. (1960, January). Internal atmospheric gravity waves at ionospheric  
 811 heights. *Canadian Journal of Physics*, *38*, 1441. doi: 10.1139/p60-150
- 812 Huang, C.-S., & Kelley, M. C. (1996, January). Nonlinear evolution of equatorial  
 813 spread F. 1. On the role of plasma instabilities and spatial resonance associ-  
 814 ated with gravity wave seeding. *Journal of Geophysical Research*, *101*(A1),  
 815 283-292. doi: 10.1029/95JA02211
- 816 Huang, C. Y., Helmboldt, J. F., Park, J., Pedersen, T. R., & Willemann, R. (2019,  
 817 March). Ionospheric Detection of Explosive Events. *Reviews of Geophysics*,  
 818 *57*(1), 78-105. doi: 10.1029/2017RG000594
- 819 Huba, J. D., Drob, D. P., Wu, T. W., & Makela, J. J. (2015, July). Model-  
 820 ing the ionospheric impact of tsunami-driven gravity waves with SAMI3:  
 821 Conjugate effects. *Geophysical Research Letters*, *42*(14), 5719-5726. doi:  
 822 10.1002/2015GL064871
- 823 Huba, J. D., & Liu, H. L. (2020, July). Global Modeling of Equatorial Spread F  
 824 with SAMI3/WACCM-X. *Geophysical Research Letters*, *47*(14), e88258. doi:  
 825 10.1029/2020GL088258
- 826 Hysell, D. L., Kelley, M. C., Swartz, W. E., & Woodman, R. F. (1990, October).  
 827 Seeding and layering of equatorial spread F by gravity waves. *Journal of*  
 828 *Geophysical Research*, *95*, 17253-17260. doi: 10.1029/JA095iA10p17253
- 829 Immel, T. J., England, S. L., Mende, S. B., Heelis, R. A., Englert, C. R., Edelstein,  
 830 J., ... Sirk, M. M. (2018, February). The Ionospheric Connection Explorer  
 831 Mission: Mission Goals and Design. *Space Science Review*, *214*(1), 13. doi:  
 832 10.1007/s11214-017-0449-2
- 833 Inchin, P. Â. A., Snively, J. Â. B., Zettergren, M. Â. D., Komjathy, A., Verkho-  
 834 glyadova, O. Â. P., & Tulasi Ram, S. (2020, April). Modeling of Ionospheric  
 835 Responses to Atmospheric Acoustic and Gravity Waves Driven by the 2015  
 836 Nepal Mw7.8 Gorkha Earthquake. *Journal of Geophysical Research: Space*  
 837 *Physics*, *125*(4), e27200. doi: 10.1029/2019JA027200
- 838 Janowiak, J., Joyce, B., & Xie, P. (2017). *Ncep/cpc l3 half hourly 4km global (60s -*

- 839       60n) merged in v1. NASA Goddard Earth Sciences Data and Information Ser-  
840       vices Center. doi: 10.5067/P4HZB9N27EKU
- 841       Jin, H., Zou, S., Chen, G., Yan, C., Zhang, S., & Yang, G. (2018, June). Formation  
842       and Evolution of Low-Latitude F Region Field-Aligned Irregularities Dur-  
843       ing the 7-8 September 2017 Storm: Hainan Coherent Scatter Phased Array  
844       Radar and Digisonde Observations. *Space Weather*, 16(6), 648-659. doi:  
845       10.1029/2018SW001865
- 846       Kakinami, Y., Kamogawa, M., Tanioka, Y., Watanabe, S., Riadi Gusman, A., Liu,  
847       J.-Y., ... Mogi, T. (2012, January). Tsunamigenic ionospheric hole. *Geophysi-  
848       cal Research Letters*, 39, L00G27. doi: 10.1029/2011GL050159
- 849       Kamogawa, M., Kanaya, T., Orihara, Y., Toyoda, A., Suzuki, Y., Togo, S., & Liu,  
850       J.-Y. (2015, November). Does an ionospheric hole appear after an inland  
851       earthquake? *Journal of Geophysical Research: Space Physics*, 120(11), 9998-  
852       10. doi: 10.1002/2015JA021476
- 853       Karan, D. K., Daniell, R. E., England, S. L., Martinis, C. R., Eastes, R. W., Burns,  
854       A. G., & McClintock, W. E. (2020, September). First Zonal Drift Velocity  
855       Measurement of Equatorial Plasma Bubbles (EPBs) From a Geostationary  
856       Orbit Using GOLD Data. *Journal of Geophysical Research: Space Physics*,  
857       125(9), e28173. doi: 10.1029/2020JA028173
- 858       Katzmazi-Joseph, Z. T., Habarulema, J. B., & Hernández-Pajares, M. (2017, Septem-  
859       ber). Midlatitude postsunset plasma bubbles observed over Europe during in-  
860       tense storms in April 2000 and 2001. *Space Weather*, 15(9), 1177-1190. doi: 10  
861       .1002/2017SW001674
- 862       Kelley, M. C., Haerendel, G., Kappler, H., Valenzuela, A., Balsley, B. B., Carter,  
863       D. A., ... Torbert, R. (1976, August). Evidence for a Rayleigh-Taylor type in-  
864       stability and upwelling of depleted density regions during equatorial spread F.  
865       *Geophysical Research Letters*, 3(8), 448-450. doi: 10.1029/GL003i008p00448
- 866       Kil, H., & Lee, W. K. (2013, July). Are plasma bubbles a prerequisite for the for-  
867       mation of broad plasma depletions in the equatorial F region? *Geophysical Re-  
868       search Letters*, 40(14), 3491-3495. doi: 10.1002/grl.50693
- 869       Kil, H., Paxton, L. J., & Oh, S.-J. (2009, June). Global bubble distribution  
870       seen from ROCSAT-1 and its association with the evening prereversal en-  
871       hancement. *Journal of Geophysical Research*, 114(A6), A06307. doi:  
872       10.1029/2008JA013672
- 873       Knudsen, D. J., Burchill, J. K., Buchert, S. C., Eriksson, A. I., Gill, R., Wahlund,  
874       J. E., ... Moffat, B. (2017, February). Thermal ion imagers and Langmuir  
875       probes in the Swarm electric field instruments. *Journal of Geophysical Re-  
876       search: Space Physics*, 122(2), 2655-2673. doi: 10.1002/2016JA022571
- 877       Komjathy, A., Galvan, D. A., Stephens, P., Butala, M. D., Akopian, V., Wilson,  
878       B., ... Hickey, M. (2012, December). Detecting ionospheric TEC pertur-  
879       bations caused by natural hazards using a global network of GPS receivers:  
880       The Tohoku case study. *Earth, Planets and Space*, 64(12), 1287-1294. doi:  
881       10.5047/eps.2012.08.003
- 882       Komjathy, A., Yang, Y.-M., Meng, X., Verkhoglyadova, O., Mannucci, A. J., &  
883       Langley, R. B. (2016). Review and perspectives: Understanding natural-  
884       hazards-generated ionospheric perturbations using gps measurements and cou-  
885       pled modeling. *Radio Science*, 51(7), 951-961. doi: https://doi.org/10.1002/  
886       2015RS005910
- 887       Krall, J., Huba, J. D., & Fritts, D. C. (2013, February). On the seeding of equatorial  
888       spread F by gravity waves. *Geophysical Research Letters*, 40(4), 661-664. doi:  
889       10.1002/grl.50144
- 890       Kudeki, E., Akgiray, A., Milla, M., Chau, J. L., & Hysell, D. L. (2007, December).  
891       Equatorial spread-F initiation: Post-sunset vortex, thermospheric winds, grav-  
892       ity waves. *Journal of Atmospheric and Solar-Terrestrial Physics*, 69(17-18),  
893       2416-2427. doi: 10.1016/j.jastp.2007.04.012

- 894 Le, G., Liu, G., Yizengaw, E., & Englert, C. (2022). Intense Equatorial Electrojet  
895 and Counter Electrojet caused by the 15 January 2022 Tonga Volcanic Eruption:  
896 Space and Ground-based Observations. *Earth and Space Science Open*  
897 *Archive*. doi: 10.1002/essoar.10511040.2
- 898 Lee, W. K., Kil, H., Kwak, Y.-S., Paxton, L. J., Zhang, Y., Galkin, I., & Batista,  
899 I. S. (2014, January). Equatorial broad plasma depletions associated with  
900 the enhanced fountain effect. *Journal of Geophysical Research: Space Physics*,  
901 *119*(1), 402-410. doi: 10.1002/2013JA019137
- 902 Li, G., Ning, B., Liu, L., Wan, W., & Liu, J. Y. (2009, January). Effect of magnetic  
903 activity on plasma bubbles over equatorial and low-latitude regions in East  
904 Asia. *Annales Geophysicae*, *27*(1), 303-312. doi: 10.5194/angeo-27-303-2009
- 905 Lin, J.-T., Rajesh, P. K., Lin, C. C. H., Chou, M.-Y., Liu, J.-Y., Yue, J., ... Kung,  
906 M.-M. (2022). Rapid Conjugate Appearance of the Giant Ionospheric Lamb  
907 Wave in the Northern Hemisphere After Hunga-Tonga Volcano Eruptions.  
908 *Earth and Space Science Open Archive*, 18. doi: 10.1002/essoar.10510440.2
- 909 Lindzen, R. S., & Blake, D. (1972, January). Lamb waves in the presence of realistic  
910 distributions of temperature and dissipation. *Journal of Geophysical Research*,  
911 *77*(12), 2166. doi: 10.1029/JC077i012p02166
- 912 Liu, C. H., Klostermeyer, J., Yeh, K. C., Jones, T. B., Robinson, T., Holt, O., ...  
913 Kersley, L. (1982, August). Global dynamic responses of the atmosphere to  
914 the eruption of Mount St. Helens on May 18, 1980. *Journal of Geophysical*  
915 *Research*, *87*(A8), 6281-6290. doi: 10.1029/JA087iA08p06281
- 916 Liu, J. Y., Tsai, Y. B., Chen, S. W., Lee, C. P., Chen, Y. C., Yen, H. Y., ... Liu, C.  
917 (2006, January). Giant ionospheric disturbances excited by the M9.3 Sumatra  
918 earthquake of 26 December 2004. *Geophysical Research Letters*, *33*(2), L02103.  
919 doi: 10.1029/2005GL023963
- 920 Ma, G., & Maruyama, T. (2006, November). A super bubble detected by dense  
921 GPS network at east Asian longitudes. *Geophysical Research Letters*, *33*(21),  
922 L21103. doi: 10.1029/2006GL027512
- 923 Makela, J. J., Vadas, S. L., Muryanto, R., Duly, T., & Crowley, G. (2010, July). Pe-  
924 riodic spacing between consecutive equatorial plasma bubbles. *Geophysical Re-*  
925 *search Letters*, *37*(14), L14103. doi: 10.1029/2010GL043968
- 926 Meng, X., Verkhoglyadova, O. P., Komjathy, A., Savastano, G., & Mannucci, A. J.  
927 (2018, September). Physics-Based Modeling of Earthquake-Induced Iono-  
928 spheric Disturbances. *Journal of Geophysical Research: Space Physics*, *123*(9),  
929 8021-8038. doi: 10.1029/2018JA025253
- 930 Nakashima, Y., Heki, K., Takeo, A., Cahyadi, M. N., Aditiya, A., & Yoshizawa, K.  
931 (2016, January). Atmospheric resonant oscillations by the 2014 eruption of the  
932 Kelud volcano, Indonesia, observed with the ionospheric total electron contents  
933 and seismic signals. *Earth and Planetary Science Letters*, *434*, 112-116. doi:  
934 10.1016/j.epsl.2015.11.029
- 935 Nishida, K., Kobayashi, N., & Fukao, Y. (2014, January). Background Lamb waves  
936 in the Earth's atmosphere. *Geophysical Journal International*, *196*(1), 312-316.  
937 doi: 10.1093/gji/ggt413
- 938 Nishioka, M., Tsugawa, T., Kubota, M., & Ishii, M. (2013, November). Concentric  
939 waves and short-period oscillations observed in the ionosphere after the 2013  
940 Moore EF5 tornado. *Geophysical Research Letters*, *40*(21), 5581-5586. doi:  
941 10.1002/2013GL057963
- 942 Otsuka, Y., Kotake, N., Tsugawa, T., Shiokawa, K., Ogawa, T., Effendy, ... Ko-  
943 molmis, T. (2006, February). GPS detection of total electron content varia-  
944 tions over Indonesia and Thailand following the 26 December 2004 earthquake.  
945 *Earth, Planets and Space*, *58*, 159-165. doi: 10.1186/BF03353373
- 946 Pi, X., Mannucci, A. J., Lindqwister, U. J., & Ho, C. M. (1997, September). Mon-  
947 itoring of global ionospheric irregularities using the Worldwide GPS Network.  
948 *Geophysical Research Letters*, *24*(18), 2283-2286. doi: 10.1029/97GL02273

- 949 Retterer, J. M., & Roddy, P. (2014, May). Faith in a seed: on the origins of equato-  
 950 rial plasma bubbles. *Annales Geophysicae*, *32*(5), 485-498. doi: 10.5194/angeo-  
 951 -32-485-2014
- 952 Rideout, W., & Coster, A. (2006). Automated gps processing for global total elec-  
 953 tron content data. *GPS Solut.*, *10*(3), 219-228. doi: 10.1007/s10291-006-0029-  
 954 -5
- 955 Rishbeth, H. (1971, February). The F-layer dynamo. *Planet. Space Sci.*, *19*(2), 263-  
 956 267. doi: 10.1016/0032-0633(71)90205-4
- 957 Roberts, D. H., Klobuchar, J. A., Fougere, P. F., & Hendrickson, D. H. (1982, Au-  
 958 gust). A large-amplitude traveling ionospheric disturbance produced by the  
 959 May 18, 1980, explosion of Mount St. Helens. *Journal of Geophysical Research*,  
 960 *87*(A8), 6291-6301. doi: 10.1029/JA087iA08p06291
- 961 Rolland, L. M., Lognonné, P., Astafyeva, E., Kherani, E. A., Kobayashi, N., Mann,  
 962 M., & Munekane, H. (2011, July). The resonant response of the ionosphere im-  
 963 aged after the 2011 off the Pacific coast of Tohoku Earthquake. *Earth, Planets*  
 964 *and Space*, *63*(7), 853-857. doi: 10.5047/eps.2011.06.020
- 965 Rottger, J. (1981, June). Equatorial spread-F by electric fields and atmospheric  
 966 gravity waves generated by thunderstorms. *Journal of Atmospheric and Ter-*  
 967 *restrial Physics*, *43*, 453-462. doi: 10.1016/0021-9169(81)90108-2
- 968 Saito, A., Tsugawa, T., Otsuka, Y., Nishioka, M., Iyemori, T., Matsumura, M., ...  
 969 Choosakul, N. (2011, July). Acoustic resonance and plasma depletion de-  
 970 tected by GPS total electron content observation after the 2011 off the Pacific  
 971 coast of Tohoku Earthquake. *Earth, Planets and Space*, *63*(7), 863-867. doi:  
 972 10.5047/eps.2011.06.034
- 973 Savastano, G., Komjathy, A., Verkhoglyadova, O., Mazzoni, A., Crespi, M., Wei, Y.,  
 974 & Mannucci, A. J. (2017, April). Real-Time Detection of Tsunami Ionospheric  
 975 Disturbances with a Stand-Alone GNSS Receiver: A Preliminary Feasibility  
 976 Demonstration. *Scientific Reports*, *7*, 46607. doi: 10.1038/srep46607
- 977 Savitzky, A., & Golay, M. J. E. (1964, January). Smoothing and differentiation  
 978 of data by simplified least squares procedures. *Analytical Chemistry*, *36*, 1627-  
 979 1639.
- 980 Shinagawa, H., Tsugawa, T., Matsumura, M., Iyemori, T., Saito, A., Maruyama,  
 981 T., ... Otsuka, Y. (2013, October). Two-dimensional simulation of iono-  
 982 spheric variations in the vicinity of the epicenter of the Tohoku-oki earthquake  
 983 on 11 March 2011. *Geophysical Research Letters*, *40*(19), 5009-5013. doi:  
 984 10.1002/2013GL057627
- 985 Shiokawa, K., Otsuka, Y., Ogawa, T., & Wilkinson, P. (2004, September). Time  
 986 evolution of high-altitude plasma bubbles imaged at geomagnetic con-  
 987 jugate points. *Annales Geophysicae*, *22*(9), 3137-3143. doi: 10.5194/  
 988 angeo-22-3137-2004
- 989 Shults, K., Astafyeva, E., & Adourian, S. (2016, October). Ionospheric detection  
 990 and localization of volcano eruptions on the example of the April 2015 Calbuco  
 991 events. *Journal of Geophysical Research: Space Physics*, *121*(10), 10,303-  
 992 10,315. doi: 10.1002/2016JA023382
- 993 Singh, S., Johnson, F. S., & Power, R. A. (1997, April). Gravity wave seeding of  
 994 equatorial plasma bubbles. *Journal of Geophysical Research*, *102*(A4), 7399-  
 995 7410. doi: 10.1029/96JA03998
- 996 Spicher, A., Cameron, T., Grono, E. M., Yakymenko, K. N., Buchert, S. C., Clausen,  
 997 L. B. N., ... Moen, J. I. (2015, January). Observation of polar cap patches  
 998 and calculation of gradient drift instability growth times: A Swarm case study.  
 999 *Geophysical Research Letters*, *42*(2), 201-206. doi: 10.1002/2014GL062590
- 1000 Sultan, P. J. (1996, December). Linear theory and modeling of the Rayleigh-Taylor  
 1001 instability leading to the occurrence of equatorial spread F. *Journal of Geo-*  
 1002 *physical Research*, *101*(A12), 26875-26892. doi: 10.1029/96JA00682
- 1003 Takahashi, H., Taylor, M. J., Pautet, P. D., Medeiros, A. F., Gobbi, D., Wrasse,

- 1004 C. M., ... Fritts, D. C. (2009, April). Simultaneous observation of  
 1005 ionospheric plasma bubbles and mesospheric gravity waves during the  
 1006 SpreadFEx Campaign. *Annales Geophysicae*, 27(4), 1477-1487. doi:  
 1007 10.5194/angeo-27-1477-2009
- 1008 Takahashi, H., Wrasse, C. M., Otsuka, Y., Ivo, A., Gomes, V., Paulino, I., ... Sh-  
 1009 iokawa, K. (2015, August). Plasma bubble monitoring by TEC map and 630  
 1010 nm airglow image. *Journal of Atmospheric and Solar-Terrestrial Physics*, 130,  
 1011 151-158. doi: 10.1016/j.jastp.2015.06.003
- 1012 Themens, D. R., Watson, C., Žagar, N., Vasylyevych, S., Elvidge, S., McCaffrey,  
 1013 A., ... Jayachandran, P. (2022). Global propagation of ionospheric distur-  
 1014 bances associated with the 2022 tonga volcanic eruption. *Geophysical Research*  
 1015 *Letters*, 49, e2022GL098158. doi: <https://doi.org/10.1029/2022GL098158>
- 1016 Tsugawa, T., Saito, A., Otsuka, Y., Nishioka, M., Maruyama, T., Kato, H., ...  
 1017 Murata, K. T. (2011, July). Ionospheric disturbances detected by GPS  
 1018 total electron content observation after the 2011 off the Pacific coast of  
 1019 Tohoku Earthquake. *Earth, Planets and Space*, 63(7), 875-879. doi:  
 1020 10.5047/eps.2011.06.035
- 1021 Tsunoda, R. T. (2010, May). On seeding equatorial spread F: Circular grav-  
 1022 ity waves. *Geophysical Research Letters*, 37(10), L10104. doi: 10.1029/  
 1023 2010GL043422
- 1024 Tsunoda, R. T., Yamamoto, M., Tsugawa, T., Hoang, T. L., Tulasi Ram, S.,  
 1025 Thampi, S. V., ... Nagatsuma, T. (2011, October). On seeding, large-scale  
 1026 wave structure, equatorial spread F, and scintillations over Vietnam. *Geophys-  
 1027 ical Research Letters*, 38(20), L20102. doi: 10.1029/2011GL049173
- 1028 Tulasi Ram, S., Rama Rao, P. V. S., Prasad, D. S. V. V. D., Niranjana, K., Gopi Kr-  
 1029 ishna, S., Sridharan, R., & Ravindran, S. (2008, July). Local time dependent  
 1030 response of postsunset ESF during geomagnetic storms. *Journal of Geophysical*  
 1031 *Research: Space Physics*, 113(A7), A07310. doi: 10.1029/2007JA012922
- 1032 Vierinen, J., Coster, A. J., Rideout, W. C., Erickson, P. J., & Norberg, J. (2016).  
 1033 Statistical framework for estimating GNSS bias. *Atmospheric Measurement*  
 1034 *Techniques*, 9, 1303-1312. doi: 10.5194/amt-9-1303-2016
- 1035 Yeh, K. C., & Liu, C. H. (1974, May). Acoustic-Gravity Waves in the Upper At-  
 1036 mosphere. *Reviews of Geophysics and Space Physics*, 12, 193. doi: 10.1029/  
 1037 RG012i002p00193
- 1038 Zakharenkova, I., Cherniak, I., & Krankowski, A. (2019). Features of storm-induced  
 1039 ionospheric irregularities from ground-based and spaceborne gps observa-  
 1040 tions during the 2015 st. patrick's day storm. *Journal of Geophysical Re-  
 1041 search: Space Physics*, 124(12), 10728-10748. doi: [https://doi.org/10.1029/  
 1042 2019JA026782](https://doi.org/10.1029/2019JA026782)
- 1043 Zettergren, M. D., Snively, J. B., Komjathy, A., & Verkhoglyadova, O. P. (2017,  
 1044 February). Nonlinear ionospheric responses to large-amplitude infrasonic-  
 1045 acoustic waves generated by undersea earthquakes. *Journal of Geophysical*  
 1046 *Research: Space Physics*, 122(2), 2272-2291. doi: 10.1002/2016JA023159
- 1047 Zhang, S.-R., Erickson, P. J., Coster, A. J., Rideout, W., Vierinen, J., Jonah, O., &  
 1048 Goncharenko, L. P. (2019, December). Subauroral and Polar Traveling Iono-  
 1049 spheric Disturbances During the 7-9 September 2017 Storms. *Space Weather*,  
 1050 17(12), 1748-1764. doi: 10.1029/2019SW002325
- 1051 Zhang, S.-R., Erickson, P. J., Goncharenko, L. P., Coster, A. J., Rideout, W., &  
 1052 Vierinen, J. (2017, December). Ionospheric Bow Waves and Perturbations  
 1053 Induced by the 21 August 2017 Solar Eclipse. *Geophysical Research Letters*,  
 1054 44(24), 12,067-12,073. doi: 10.1002/2017GL076054
- 1055 Zhang, S.-R., Vierinen, J., Aa, E., Goncharenko, L. P., Erickson, P. J., Rideout, W.,  
 1056 ... Spicher, A. (2022). 2022 Tonga volcanic eruption induced global propaga-  
 1057 tion of ionospheric disturbances via Lamb waves. *Frontiers in Astronomy and*  
 1058 *Space Sciences*, 15. doi: 10.3389/fspas.2022.871275